

ABSTRACT

AMAN, RONALD LEE. Evaluation and Modeling of Biodegradable Metallic Implants for Load-based Fixation. (Under the direction of Ola L. A. Harrysson and Denis R. Cormier.)

Biodegradable metal implant research is increasing in importance as a possible means to reduce complications associated with multiple surgeries in cases where load based fixation is necessary, but long term physical constraint of bone tissue is problematic. Recent advances in metallurgical studies of magnesium alloys have shown promise for their use as biodegradable implants, but the results of *in vitro* studies vary widely and do not compare well with *in vivo* studies.

This research focuses on quantifying the strength performance of a magnesium alloy over time in a balanced salt solution and modeling the performance to optimize implant performance *in vivo*. Two studies were undertaken. In the first study, three different magnesium plate configurations were evaluated: solid, small holes simulating a porous structure, and large-hole samples simulating a bone plate. Samples were subject to varying lengths of submersion from 0 to 20 weeks in Hanks Balanced Salt Solution at the common human body temperature of 37 degrees Celsius and tested using a four-point bend test. The results indicate slow degradation of the proof load (0.2% offset) over time with a corresponding decrease in average bending stiffness. Corrosion product accumulation caused a gain in mass over time as expected, with the large-hole configuration accumulating the most and the no-hole samples accumulating the least. Small-hole configured samples were similar in mass gain to the large-hole samples. The small-hole and large-hole samples lost approximately 25% of their strength over the 20 week test period and the no-hole samples lost approximately 10%.

In the second study, bone constructs consisting of simulated bone (polyacetal Delrin[®]), AZ31 alloy bone plates, and AZ31 bone screws were subjected to corrosion fatigue testing while immersed in Hanks Balanced Salt Solution for varying lengths of time. The test system imparted three different load mechanisms in 4 point bending orientation to 5 samples each over test durations of 0, 2, 4, 6, 8, 10, 14, 16, and 20 weeks. One set of samples was subjected to static loading, another set to dynamic or cyclic loading and the third set to no-load condition. After the corrosion process, corrosion products were removed via chromic acid etching and samples weighed and tested in a 4-point bend test. Bending strength, bending stiffness, and mass loss per week were recorded and compared for each sample.

A mathematical model of the corrosion of AZ31 magnesium alloy was developed to estimate the service life of a resorbable implant. The bending stiffness of previously tested constructs was used to derive a change in the cross sectional area of inertia. The change in cross sectional area of inertia is assumed to be the result of corrosion, and simplifying assumptions of rectangular cross section and pitting corrosion approximating general corrosion allow the derivation of a corrosion penetration model. By applying an estimate of corrosion penetration, the estimate of bending strength can be calculated. The derived model is tested against 2 sets of data, one with corrosion media exposure to 3 sides of a construct, and one with 4 sides exposed. The model agrees within 30% of testing results, and is applicable to any corrosion medium and any alloy as long as corrosion rate estimates are known. The corrosion model may be applied to situations where the corrosion process is not consistent, as is the case with magnesium plates in contact with soft tissue or cortical bone.

Evaluation and Modeling of Biodegradable Metallic Implants for Load-based Fixation

by
Ronald Lee Aman

A dissertation submitted to the Graduate Faculty of
North Carolina State University
in partial fulfillment of the
requirements for Degree of
Doctor of Philosophy

Industrial Engineering

Raleigh, North Carolina

2013

APPROVED BY:

Harvey A. West

C. Thomas Culbreth

Denis Marcellin-Little

Denis R. Cormier
Co-chair of Advisory Committee

Ola L.A. Harrysson
Chair of Advisory Committee

DEDICATION

To my wife Erica and my son Cody,
whose unwavering love, support, and sacrifice
gave me the strength to complete this dissertation.

BIOGRAPHY

Ron is a two time graduate of North Carolina State University's Edward P. Fitts Department of Industrial and Systems Engineering (B.S. 2002, M.S. 2004). His masters' work focused on reverse engineering complex free-form surfaces and specifically aligning point cloud data from overlapping scan areas.

In 2004, Ron began Ph.D. studies and in 2005 took a full time Research Assistant position in the Furniture Manufacturing and Management Center at N.C. State University. During this time he participated in research related to furniture manufacturing, advanced manufacturing, additive manufacturing and was responsible for teaching undergraduate classes as well as managing manufacturing and computing laboratories. During this time Ron became interested in additive manufacturing and began research in two-phase electron beam melting, attempting to create metal matrix composites in a layer by layer process.

His research interest broadened to include biomedical applications of additive manufacturing. His dissertation work laid the groundwork for customized biomedical implants which can be custom tailored for each individual application.

After completing his Ph.D. degree from N.C. State in the summer of 2013 he plans to focus on improving additive manufacturing processes and extending the work done on his dissertation by developing additive processes which allow functionally graded biomedical implant materials customized for each application. In addition, Ron is interested in improving current systems and developing new additive manufacturing processes which reduce custom part costs, improve mechanical properties and accuracy of additive parts, and

include multiple materials for embedding multi-functional systems in one manufacturing process.

ACKNOWLEDGEMENTS

The work presented in this dissertation is the culmination of a long journey which would not have been possible without the help of a very large number of people. The support and friendship of the people listed below is the primary reason that this work was completed, and I cannot overstate their impact on my life:

To my co-advisors, mentors and friends Denis Cormier and Ola Harrysson, whose friendship and guidance I will always be thankful, and without their significant guidance and encouragement, this work would not have been completed. Ola's dedication, drive, vast knowledge and interest in educating himself and those around him (even when seemingly they don't want to be educated) is inspiring, and will lead to many very successful graduate students. His commitment to students' success, academic integrity and progressing the state of the art are a model for all faculty to follow.

Denis' exceptional research and academic vision inspires all that come into contact with him. He is always commenting or questioning things far in advance of what seemingly would make sense; I cannot count the number of ideas I have heard Denis comment about only to see them come to fruition 3-5 years later.

To my committee, the countless discussions, recommendations and encouragements have helped immensely and I appreciate each and every interaction. Harvey West in particular has endured countless discussions of details that ultimately made this endeavor successful. His friendship and patience I will forever cherish. Denis Marcellin-Little's interest and seemingly infinite knowledge have been incredibly helpful, and I look forward to repaying

all of his efforts in the future. Tom Culbreth's willingness to help at all times and his absolute commitment to helping all students all of the time has been an incredible inspiration for me.

To Rusty King and Thom Hodgson, thank you for your inspiration, interest and helping to keep me on track. To the faculty of the Industrial and Systems Engineering department, thank you for all of the support and dedication.

To my fellow students that have had such an impact on my time here at N.C. State: Tim Horn, Molly Purser, Jessica Springer, Kyle Knowlson, Tushar Mahale, Harshad Srinivasan, Guhaprasanna Manogharan, Li Yang, and the many others that I have had the pleasure of knowing and interacting with, thank you for all you have done for me.

To Marcio Cerullo, thank you for all of your help in the nano lab. To Debbie Allgood-Staton, thank you for all of your support in making this happen.

To the Furniture Manufacturing and Management Center, this certainly would have not happened without all of the support and encouragement from those running and working in the center. To Steve Walker, thank you for all of the discussions we have had regarding the work here (and especially other things), and your encouragement to power through.

To my many friends I say thank you for always being willing to tolerate another discussion about my work. Jason and Sandy Low, Ken and Jaimee Docherty and Burak and Mary Eryigit I am especially grateful to. There are many others that supported my efforts, I am forever grateful to each and every one of you. I sincerely apologize to anyone that I have left off of this list, but you already know just how feeble my mind is.

Although the work presented in this dissertation was ‘unfunded’ I would like to extend my appreciation to those that helped find the necessary funds to make the work possible. Russell King, Ola Harrysson, Harvey West, Paul Cohen and Debbie Allgood-Staton were all instrumental in ensuring that adequate resources were available to finish the work. Thank you all for your generous support. In addition I would like to extend my appreciation to Dynamic Machining and Manufacturing for machining the simulated bone screws used in this study.

TABLE OF CONTENTS

LIST OF TABLES	x
LIST OF FIGURES	xi
1. INTRODUCTION	1
2. LITERATURE SURVEY.....	8
3. <i>IN VITRO</i> ANALYSIS OF STRENGTH AND CORROSION CHARACTERISTICS OF MAGNESIUM ALLOY (AZ31) IN HANKS SOLUTION.....	14
INTRODUCTION.....	14
METHODS AND MATERIALS	19
Methods	19
Materials	21
Sample Preparation.....	22
Test Rig Preparation.....	28
Sample Testing	33
RESULTS	36
DISCUSSION	42
RELATED AND FURTHER WORK.....	43
CONCLUSION.....	44
4. MECHANICAL PROPERTIES ANALYSIS OF AZ31 MAGNESIUM ALLOY UNDER DIFFERENT LOADING CONDITIONS IN HANKS BALANCED SALT SOLUTION	45
INTRODUCTION.....	45
MATERIALS AND METHODS	47
RESULTS	62
DISCUSSION	67
CONCLUSION.....	70
5. MODELING CORROSION OF AZ31 FOR OPTIMIZING CUSTOM OPEN REDUCTION INTERNAL FIXATION	72
INTRODUCTION.....	72
MATERIALS AND METHODS	75
MATHEMATICAL MODELING	77
RESULTS	84
DISCUSSION	86
FUTURE WORK.....	94
CONCLUSION.....	95
6. FUTURE WORK AND CONCLUSION.....	96
FUTURE WORK	96
In vivo testing	97

TABLE OF CONTENTS

Modeling	98
CONCLUSION.....	99
REFERENCES	101

LIST OF TABLES

Table 3-1 Summary of the physical and mechanical properties of various implant materials in comparison to natural bone - reproduced from (Staiger, Pietak et al. 2006)	17
Table 3-2 Composition of AZ31 Alloy.....	22
Table 3-3 Initial sample masses (grams)	27
Table 3-4 Sample statistics, mass data in grams.....	27
Table 3-5 Final sample masses, in grams	40
Table 3-6 Sample mass gain in grams with average.....	41
Table 4-1 Mass loss (grams) per week for cyclic loaded (CY), non-loaded (NL) and static loaded (ST) specimens	63
Table 4-2 Time period comparisons of weekly average mass loss given in <i>t</i> statistic values (14 df).....	63
Table 4-3 Bending strength averages (Nm) for all samples, including those that broke during corrosion process	64
Table 4-4 Bending strength averages (Nm) for all samples except those that broke during corrosion process	65
Table 5-1 Bending Strength (Nm) comparison and corrosion depth (mm) estimate for cyclic loaded samples	84
Table 5-2 Bending Strength (Nm) comparison and corrosion depth (mm) estimate for non-loaded samples	85
Table 5-3 Bending Strength (Nm) comparison and corrosion depth (mm) estimate for statically loaded samples	85
Table 5-4 Bending Strength (Nm) comparison and corrosion depth (mm) estimate for cyclically loaded samples with $y = 1.6$ mm (assumed constant throughout test)	88
Table 5-5 Bending Strength (Nm) comparison and corrosion depth (mm) estimate for non-loaded samples with $y = 1.6$ mm (assumed constant throughout test)	89
Table 5-6 Bending Strength (Nm) comparison and corrosion depth (mm) estimate for statically loaded samples with $y = 1.6$ mm (assumed constant throughout test)	89
Table 5-7 Bending strength estimates of data acquired in Chapter 3 (Nm).....	94

LIST OF FIGURES

Figure 3-1 Sample configurations: Solid, large holes, and small holes.....	23
Figure 3-2 Machining fixture in clamped position	24
Figure 3-3 Machining fixture in open position showing aligning pins.....	24
Figure 3-4 Dimensioned drawing of solid plate (top), large-hole plate (middle) and small-hole plate (bottom) (dimensions in mm)	25
Figure 3-5 Test rig configuration showing samples hanging over empty test containers.....	29
Figure 3-6 Environmental chamber used to maintain temperature conditions.....	31
Figure 3-7 Test apparatus and samples immediately after start of test.....	32
Figure 3-8 Test samples drying in environmental chamber following corrosion test and testing preparation	34
Figure 3-9 ASTM F382-99 test set up with large span of 101.6 mm and small span of 25.4 mm.....	35
Figure 3-10 ASTM F382-99 bending test during loading	35
Figure 3-11 The average 0.2% offset proof load of samples versus time (Error bars are Standard Error)	36
Figure 3-12 Average Bending Stiffness of samples versus time (Error bars are Standard Error).....	37
Figure 3-13 Average mass gain versus time, in grams, including linear trend line	39
Figure 4-1 Simulated bone plate model.....	48
Figure 4-2 Bone screw model based on a 3.5 mm cortical bone screw	49
Figure 4-3 Simulated bone segments fabricated from Delrin.....	49
Figure 4-4 Model of assembled bone construct.....	50
Figure 4-5 Assembled bone construct.....	50
Figure 4-6 Model of test platform showing four test rows with containers for 15 samples	52
Figure 4-7 Schematic of testing apparatus with construct in place	53
Figure 4-8 Test rig immediately prior to initiation of loading. Note the aluminum cylinders (background top), Delrin loading rods with radius end showing, loading blocks, and constructs. HBSS with phenol red is easily seen, along with level- controlling overflow.....	54
Figure 4-9 Top view of upper tank of test rig. Note the loading blocks with hemi-sphere machined in top and the acrylic aligning the loading blocks (numbers are written on acrylic to denote chamber position, not sample identification).....	56

LIST OF FIGURES

Figure 4-10 Assembled and operating testing rig. Note: dynamic loading is in the foreground, static loading in the background and no-load samples were in the middle	56
Figure 4-11 Testing apparatus view from above showing individual testing locations, orificed drains (center) and makeup water inlets at the sides. Note the corrosion on the samples to the right (after 2 weeks) as compared to the newly inserted 8-week samples	58
Figure 4-12 ASTM F382-99 testing set up on universal test machine	60
Figure 4-13 ASTM F382-99 4 point bend test at full displacement of a non-corroded sample	61
Figure 4-14 ASTM F382-99 4-point bend test showing permanent plastic deformation of a non-corroded sample. Crosshead returned to initiation location (Figure 4-11)	62
Figure 4-15 Average Bending Strength vs. Exposure time in weeks. Samples broken during corrosion process assumed to have bending strength of 0 (Error bars are Standard Error).....	66
Figure 4-16 Average bending strength vs. exposure time in weeks. Samples broken during corrosion process are not included	67
Figure 5-1 Cross section of simple beam with dimensions b and h , and corrosion penetration x_1 , x_2 , x_3 , and x_4 per side clockwise around the cross section	79
Figure 5-2 Graph of ΔI per mm of corrosion	82
Figure 5-3 Estimate of the surface corrosion depth for different loading conditions per exposure time.....	86
Figure 5-4 Construct with lowest measured bending stiffness (14,571 N/m) and highest implied corrosion. Visual inspection shows much less corrosion penetration than predicted (predicted > 0.84 mm, original plate thickness = 3.2 mm).....	87
Figure 5-5 Micro CT image of construct 58 (cyclic loading) after 12 weeks exposure to corroding medium. Measured pit depth is 2.11 mm, original thickness = 3.2 mm	90
Figure 5-6 View of construct from various positions. Top left is a model of the bone construct, top right is the approximate section plane of the radiographic slice in Figure 5-5, bottom is the view normal to section plane.....	91

LIST OF FIGURES

Figure 5-7 Triangulated surface model of a boolean subtraction of a non-corroded sample and a corroded sample. Data reconstructed from μ CT data	92
--	----

1. INTRODUCTION

Implants

The metallic medical implant market is growing approximately 9% per year and is currently estimated at about \$27 billion (Yun, Dong et al. 2009). These implants are used for everything from bone fixation and reconstruction to stents used to open clogged arteries and microelectronics used for stimulation, control and data collection. Nearly all of these are made from stainless steels, cobalt chromium, or titanium alloys.

Biodegradable implants have recently been increasing in popularity. Recent advances in polymer science have created implantable polymer devices which can degrade over time and release elements which the body can either use internally or dispose of through the kidneys (Pietrzak, Eppley 2000, Suuronen, Pohjonen et al. 1998), and can effectively take the place of metallic implants (Lee, Oh et al. 2010). Examples of materials currently in use include poly(lactic acid) (PLLA, PDLLA), poly(glycolic acid) (PGA), poly(caprolactone) (PCL), poly(lactic glycolic acid) (PLGA), poly(methyl methacrylate) (PMMA) and more. These materials degrade in the body through hydrolysis and are eventually eliminated through respiration and urine, and can last anywhere from a few weeks to a few years (Middleton, Tipton 2000).

Extension of bioabsorbable implants from polymers into metals and metallic alloys provides the capability of more rigid holding and stabilization (a problem with some polymer based implants (Kim, Kim et al. 2009, Araujo, Waite et al. 2001)), while eliminating the necessity of further surgical cycles to remove the implant after performing its intended role.

Biodegradable metallic alloys have been proposed using magnesium and magnesium alloys, and iron (Waksman, Pakala et al. 2008, Waksman, Pakala et al. 2007). These metals break down into corrosion products which the body can easily deal with and are, in most cases, required by the body for various biological processes. These metals have been proposed for use in bone fixation and reconstruction (bone plates) (Zhang, Xu et al. 2009), cement for implant stabilization (Yu, Wang et al. 2010), as stents (Waksman, Pakala et al. 2006), as base structures for tissue engineering (Witte, Ulrich et al. 2007, Gu, Zhou et al. 2010, Witte, Ulrich et al. 2007), and as biodegradable drug delivery vehicles (Di Mario, Griffiths et al. 2004).

Magnesium

Magnesium and magnesium alloys have long been used in many applications including chemical, pyrotechnics, and structural applications where reduced weight and moderate strength are desired properties, such as automobiles and aircraft. Chemical applications include use in the development of organic and organometallic compounds, as a neutralizer in lubricating oils, and in the purification of gasses such as hydrogen due to its high activity level. Magnesium burns bright white and is used extensively in pyrotechnics. Structural applications include aircraft and missile skins, housings for electronics, and various automobile components such as frames, brackets, panels and wheels (Avedsian, Baker 1999). Of historical note, in 1936 the Volkswagen Beetle became the first production car to use cast magnesium and magnesium alloys extensively – the crankcase and transmission housing,

among other components, were made from magnesium - and led to Volkswagen being the world's largest consumer of magnesium in the 1960s and 1970s.

Magnesium is a common element found nearly everywhere on the earth, but not in its elemental state due to its high reactivity. Instead it is found as magnesium oxide (MgO) or magnesium chloride (MgCl₂) and must be purified; normally using electrolysis of brine salts (Avedsian, Baker 1999). Approximately 68% of the magnesium produced in 1997 was used in alloying with either aluminum (~50%) or ferrous alloys (Avedsian, Baker 1999). Only approximately 30% was used in structural applications with die-casting being the major product (Avedsian, Baker 1999).

Pure magnesium has a density of 1.74 grams per cubic centimeter (g/cc) and compares to aluminum with a density of 2.70 g/cc and steels with densities greater than 7.7 g/cc. Magnesium has a melting point of 650 °C, Young's modulus of 45 GPa, and has a hexagonal crystal structure, meaning it is a relatively brittle metal. Magnesium is highly flammable and while easy to ignite in thin strips or powder is somewhat difficult to ignite in bulk. Once ignited, burning magnesium is very difficult to extinguish and typically requires suffocation using sand or earth.

Magnesium is the fourth most abundant mineral in the human body according to the National Institutes of Health (NIH). The NIH reports:

Magnesium is needed for more than 300 biochemical reactions in the body. It helps maintain normal muscle and nerve function, keeps heart rhythm steady, supports a healthy immune system, and keeps bones strong. Magnesium also helps

regulate blood sugar levels, promotes normal blood pressure, and is known to be involved in energy metabolism and protein synthesis. There is an increased interest in the role of magnesium in preventing and managing disorders such as hypertension, cardiovascular disease, and diabetes. Dietary magnesium is absorbed in the small intestines. Magnesium is excreted through the kidneys. (National Institutes of Health 2009)

While dietary magnesium is essential to proper body function (Romani, Scarpa 2000, Rubin 2005, Rubin 2005), excess magnesium levels may be dangerous with symptoms including nausea, diarrhea, muscle weakness, extremely low blood pressure and irregular heartbeat. Magnesium is stored primarily in bones and is excreted through the kidneys when excess levels exist (National Institutes of Health 2009).

Alloying Agents

Magnesium alloys can be broadly broken down into three categories; pure magnesium with trace elements added, alloys containing aluminum (Zhang, Xu et al. 2009, Witte, Kaese et al. 2005, Witte, Fischer et al. 2006, Wen, Wu et al. 2009) and those free of aluminum. Alloying elements are generally added to improve the strength, fatigue resistance or corrosion resistance, or a combination of these properties. Magnesium alloys conform to the naming conventions outlined by ASTM using letter-figure combinations.

Popular commercially available alloys include AZ31 and AZ91 (Witte, Kaese et al. 2005), as well as AE21, LAE442 and AE42. AZ alloys contain aluminum and zinc (3% and 1% respectively for AZ31 and 9% and 1% respectively for AZ91), AE and LAE alloys contain aluminum and rare-earth elements and a small amount of manganese. AZ91 and

AZ31 are popular alloys often found in aerospace applications, and are available in cast, forged forms or as rolled sheets. The addition of aluminum improves strength and hardness and makes the alloy easier to cast. Zinc is added, especially in combination with aluminum, to improve strength at room temperature. With aluminum concentrations greater than 6% the alloy becomes heat treatable.

Alloys free of aluminum often contain rare-earth metals to improve strength at elevated temperatures. They also reduce weld cracking and improve porosity due to the elements' effect on narrowing the freezing range of the alloy. Rare-earth elements normally are added in one of two forms, mischmetal or didymium. Mischmetal is a naturally occurring mixture of approximately 50% cerium and 50% lanthanum and neodymium, and didymium is a natural mixture of approximately 85% neodymium and 15% praseodymium.

Magnesium as an Implant

Magnesium has recently gained favor for use as an implant in certain applications. The most advanced application to this point focuses on the use of magnesium alloys for cardiovascular stents (Waksman et al. 2006, Waksman et al. 2007, Waksman et al. 2009, Di Mario et al. 2004, Erbel et al. 2007). The primary motivation for using magnesium is to avoid subsequent medical procedures to remove the implant upon completion of its primary mission. In certain situations it is undesirable to leave metallic implants in place such as in cases where it may interfere with bone growth as in young children, or when long-term exposure to wear or corrosion products may cause complications (Lhotka, Szekeres et al. 2003).

Magnesium and magnesium alloys generally corrode slowly in air (Song, Atrens 2004). However in environments which include chlorides in an electrolytic solution, such as the situation in the human body and saltwater, the corrosion rate is markedly higher. In fact, magnesium is often used as a sacrificial anode in these environments to protect other metals from corrosion. The corrosion rate in these environments can be controlled through several means: coatings applied to reduce fluid contact with the magnesium surface, impressed current, modification of the specific alloy or processing method, or control of the surrounding fluid pH.

Controlling the rate of corrosion is a major research issue with regard to biodegradable metal implants. High corrosion rates may cause premature loss of structural integrity of the implant, high evolution rate of hydrogen gas from the corrosion process, or overload the body with corrosion products. Structural integrity of the implant can be maintained by making the implant sufficiently large to allow for the degradation over the expected healing time. However the evolution of hydrogen is problematic because it is possible to exceed the absorption rate of the body, and may need to be removed by external means (i.e. needle extraction). The overall hydrogen adsorption rate in rats was 0.954 mL/hr (Piiper, Canfield et al. 1962), thus keeping hydrogen evolution less than this rate will minimize the likelihood of subcutaneous gas bubble formation. Optimizing the size, shape and alloy composition of potential implants is important to the success of biodegradable metallic implants and to the recipient's physiological response to the implant.

This study was undertaken to evaluate the mechanical performance of AZ31 over time in a corrosive environment which more accurately reflects the expected conditions *in*

vivo. The corrosive environment simulated the conditions that an implant would be expected to endure during the healing process of a long bone fracture when used for fixation. The evaluation started with immersion corrosion testing of three plate configurations in static balanced salt solution for a period of 20 weeks. The mechanical performance based on this study suggested that AZ31 was a possible candidate for an implant material. A second study was commissioned to evaluate the mechanical performance of a simulated fixation system which consisted of magnesium alloy plates and screws attached to two segments of simulated bone. This test incorporated three different loading configurations which simulated moderate activity during the healing process (cyclic loading), assembly in a loaded, non-active configuration (static loading), and a control group with no load applied. The results of this test showed it was important to consider the expected activity level of the patient during the healing process when designing and installing biodegradable implants based on magnesium. A third study was undertaken to model the mechanical performance of the AZ31 alloy over time in a corrosive environment to predict the expected functional lifetime of a biodegradable magnesium alloy implant under various loading conditions to optimize the size of the implant.

2. LITERATURE SURVEY

Magnesium was first proposed as a ligature in 1878 (Huse 1878). Polymer based ligatures did not yet exist, and the natural corrosion of magnesium in the body into magnesium hydroxide and the ability of the body to dispose of this made it an interesting candidate for use where fixation was required for limited periods of time. No subsequent operations to remove the ligature were required as the magnesium corroded away over a predictable amount of time.

In 1906 pure magnesium fixation plates were introduced by Lambotte (Witte et al. 2010). The plates were fixated using steel screws and resulted in rapid degradation, presumably through galvanic corrosion, within eight days. A small amount of work was done in the early part of the 20th century (McBride 1938), but interest soon faded in favor of stainless steel alloys which became available mid-century.

There has been renewed interest in magnesium as a biodegradable implant, and new alloys have been developed to reduce the high corrosion rate. Studies that compared different testing media (*in vitro*) (Xin et al. 2010) and alloys (Gu et al. 2009) showed widely variable results, and have not been consistent with *in vivo* results.

Biological Performance of Magnesium Alloys

In 2006, Frank Witte and others from the Hanover Medical School performed a study of two cast magnesium alloys (AZ91 and LAE442) in accordance with the ASTM standard corrosion tests comparing corrosion performance both *in vitro* and *in vivo* (Witte, Fischer et al. 2006). Their findings show that the ASTM standard corrosion tests are not well suited to

predict *in vivo* corrosion results. In fact, the *in vivo* corrosion rate was about four orders of magnitude lower than *in vitro* results. *In vitro* testing consisted of placing several samples in a 25 liter solution of NaCl, MgSO₄, MgCl₂, CaCl₂, in accordance with ASTM –D1141-98 for 24, 96, 192 and 240 hours at room temperature. *In vivo* corrosion rates were estimated by approximating the implant volume using voxelation of a 3D computer model reconstructed from 2D image layers captured using synchrotron-radiation-based microtomography (SR μ CT). The 1.5 mm by 20 mm implants, cast then machined magnesium alloys, were in service for 18 weeks in the femora of guinea pigs. *In vivo* corrosion rates were estimated at 1.21×10^{-4} mm/year and 3.52×10^{-4} mm/year for LAE442 and AZ91D respectively. There are some questions regarding the controls used to determine the difference between *in vivo* and *in vitro* corrosion rates in this paper (Kannan, Raman 2008), including the use of simulated seawater used in the *in vitro* test and the temperature at which the *in vitro* test was carried out. It should be noted that it is well known that the corrosion rate increases with increased temperature in magnesium alloys, thus the *in vitro* corrosion rate in this study may very well be underestimated.

In 2009, Wang, Shinohara, Zhang and Iwai characterized the surface products of AZ31 alloy corroded in a sodium chloride solution. They found three distinct main layers of corrosion products consisting of primarily magnesium at the substrate, MgO in the middle layer, and Mg(OH)₂ and MgO in the outer layer (Wang, Shinohara et al. 2009). In addition, MgCO₃ was found to be contained in the corrosion products in the passivation layer. Note that this test was conducted in dilute sodium chloride solution and not a simulated body fluid.

In 2008, Kannan and Raman (2008) evaluated a calcium containing magnesium alloy denoted AZ91Ca. Wu, Fan, Gao, Zhai, Zhu (2005) had previously reported that addition of calcium improved general corrosion performance and improved mechanical properties up to about 1 wt.%. The Kannan study showed that AZ91Ca (immersed in modified-Simulated Body Fluid (m-SBF)) corrosion performance and Ultimate Tensile Strength (UTS) was enhanced, when compared to a control group exposed to only air. The addition of calcium should not introduce new toxicity concerns as bone already contains large quantities of the element. Furthermore, it was suggested that the addition of calcium to the AZ91 alloy may accelerate calcium phosphate formation on the surface of the magnesium alloy, enhancing corrosion resistance and encouraging bone growth.

In 2009, Yun et al. reported that magnesium may be a suitable material for biodegradable implants after cytotoxicity experiments. MTT assay and visual observation through cell staining showed results that cells were not significantly altered in the presence of corroding magnesium (Yun et al. 2009). Magnesium samples of 99.95% purity were tested for their corrosion potential in de-ionized (DI) water, Phosphate Buffered Saline (PBS), and McCoys 5A-5% Fetal Bovine Solution (FBS). Electrochemical corrosion tests showed that DI water had the least corrosion potential and that PBS and FBS were nearly identical. The corrosion current density of PBS was greater than FBS, which is reinforced by the obvious corrosion products accumulating on the PBS sample. This can be attributed to proteins in the testing solution creating a layer which decreases corrosion activity. This phenomenon is also described in (Rettig, Virtanen 2008), where it was shown that the corrosion potential for

magnesium alloys containing rare earth elements in m-SBF is lower than in NaCl solutions, presumably caused by the addition of albumin in physiological concentrations.

In 2010, Kannan reported on the influence of microstructure on *in vitro* corrosion rates of magnesium alloys (Kannan 2010). Corrosion performance of die cast and sand cast versions of AZ91 magnesium alloy were compared to pure magnesium using potentiodynamic polarization and electrochemical impedance spectroscopy in a pH buffered Simulated Body Fluid (SBF). The pure magnesium showed less resistance to corrosion than the AZ91 alloy in either cast form. The sand cast AZ91 sample showed more resistance to corrosion than the die cast sample in contrast to previous work done in chloride containing solutions. Previous work showed that the small grain size of die cast magnesium alloys (as compared to larger sand cast grain size) improved corrosion resistance in chloride containing solutions, presumably because of the higher aluminum concentrations in the grains and a continuous network of grain boundaries. In Kannan's study, there was a difference in the aluminum concentration in the two AZ91 alloys, the sand cast alloy having a greater aluminum concentration; therefore because of the higher aluminum concentration the corrosion resistance could not be attributed to the grain size but, rather to the overall higher alloy aluminum concentration. The polarization curves did not show a meaningful difference in the corrosion current density between sand and die cast alloys, but did show pure magnesium to have a higher corrosion current density. Kannan's article contends the sand cast alloy may be a better biodegradable implant material because die cast AZ91 alloy contained a high volume fraction of β -precipitates ($\text{Mg}_{17}\text{Al}_{11}\text{Zn}_{0.5}$ (Ambat et al. 2000)) which are less

favorable for biodegradation, and the grains tend to be dissolved more rapidly in the die cast sample leading to reduced mechanical properties.

Wang, Estrin and Zuberova evaluated the corrosion performance of AZ31 processed via Squeeze Casting (SC), Hot Rolling (HR) and equal channel angular pressing (ECAP) (Wang et al. 2008). They found that the SC samples, with grain sizes on the order of 450 μm , corroded more rapidly than the HR and ECAP samples with grain sizes of 15 μm and 2.5 μm respectively. The samples were suspended in Hanks solution, which was maintained at a pH of 7, for various lengths of time up to 20 days. The corrosion rate starts out relatively high and decreases over time for all three sample materials; SC starts at approximately 2 $\mu\text{m}/\text{day}$ and decreases to less than 1 $\mu\text{m}/\text{day}$ after 20 days. Similarly, the ECAP and HR sample degradation rates start at about 1.5 $\mu\text{m}/\text{day}$ and 1.35 $\mu\text{m}/\text{day}$ respectively after 1 day and decrease to approximately 0.8 $\mu\text{m}/\text{day}$ after 20 days.

Zhang, et. al. (Zhang, Xu et al. 2009) reported an *in vivo* test that highlights the different degradation rates of magnesium alloys (Mg-Mn-Zn specifically) based on proximity to cortical and cancellous bone tissue. More degradation was noted in the marrow channel, presumably due to increased fluid access. Fibroblasts were noted at the bone/bone plate interface, but none were noted on the opposite side of the bone plate. No fibrous capsule or macrophage or giant cells were noted around the implant. Evaluation of the blood showed little change and no disorder to liver or kidneys was noted.

Zberg, Uggowitzer and Loffler (Zberg, Uggowitzer et al. 2009) recently reported a reduction of hydrogen evolution using MgZnCa glasses formed via casting. This is important to prevent subcutaneous gas bubble formation which occurs if hydrogen evolution

is greater than what the body can process. The zinc rich glasses showed a significantly denser and thinner corrosion surface after 72 hours in simulated body fluid, as compared to a porous and thicker surface for the lower zinc level samples. In addition, in animal studies, the zinc rich glasses showed no gas bubbles (implanted in soft tissue) as compared to magnesium samples which showed obvious gas bubble formation.

Several recent papers (Witte et al. 2010, Staiger et al. 2006, Kirkland et al. 2010, Witte et al. 2008, Yun et al. 2009) review the most relevant work in this area and offer a consensus opinion. Generally these papers consider magnesium alloys, particularly AZ91 and rare earth element containing alloys as the most promising biodegradable implant materials.

3. *IN VITRO* ANALYSIS OF STRENGTH AND CORROSION CHARACTERISTICS OF MAGNESIUM ALLOY (AZ31) IN HANKS SOLUTION

^aRonald L. Aman, ^bOla L. A. Harrysson, ^cDenis Marcellin-Little, ^dDenis R. Cormier, ^eHarvey A. West, ^fC. Thomas Culbreth

^a NC State University, ron_aman@ncsu.edu

^b Associate Professor, Dept. of Industrial and System Engineering, NC State University. harrysson@ncsu.edu

^c Professor, Orthopedic Surgery, College of Veterinary Medicine, NC State University. denis_marcellin@ncsu.edu

^d Professor, Department of Industrial and Systems Engineering, Rochester Institute of Technology. drceie@rit.edu

^e Research Assistant Professor, Dept. of Industrial and System Engineering, NC State University. hawest@ncsu.edu

^f Professor, Dept. of Industrial and System Engineering, NC State University. culbreth@ncsu.edu

Introduction

Currently, titanium alloys and stainless steels are used extensively in fixation and reconstruction of the skeletal system because they possess adequate strength and are essentially bio-inert. Implants made from these materials are inserted into the body and affixed to bone via screws during a surgical operation but require removal after the healing process is complete in certain applications. Secondary operations to remove these previously implanted devices increase medical care costs and can increase complications such as infections. Failure to remove these devices can cause other complications such as irritation and inflammation, release of toxic alloying elements as wear debris (Puleo, Huh 1995, Jacobs et al. 1998), or limit bone growth.

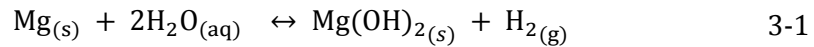
Magnesium and magnesium alloys have recently generated a significant amount of scientific interest for use in medical device implants and scaffold materials (Kirkland, Lespagnol et al. 2010, Yun, Dong et al. 2009, Staiger, Pietak et al. 2006, Witte, Eliezer et al. 2010, Gu, Zhou et al. 2010). Magnesium alloys have long been used in the aerospace and automobile industry due to their low weight (density of 1.74 g/cc) and moderate mechanical properties. However, these alloys typically have a high corrosion rate, especially in the presence of solutions containing chlorides, and are very susceptible to galvanic corrosion due to magnesium's relatively anodic position in the electromotive series (Fontana, Green 1978). It is the property of high corrosion rate that generates much interest for this material in medical implants.

Interest in metallic bio-resorbable materials for implants has increased dramatically in recent years. Recent surveys of literature show substantial increases in the number of articles regarding bio-resorbable metal implants. Articles published by year range from 15 for all years up to and including 1990, to 23 published in 1999 alone, and 81 published in 2009 (ScienceDirect.com 2010). Of particular interest are magnesium and its alloys, which have an elastic modulus close to that of natural bone. This compares favorably relative to current implant materials (Staiger et al. 2006) for load based applications (see Table 3-1).

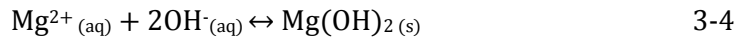
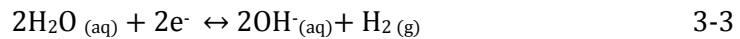
The first known documented use of magnesium internally is as a ligature in 1878 (Huse 1878). The author claimed magnesium to be superior to the then current technology due to its inorganic nature, predictable behavior, and ultimate reduction to magnesia in the body which can be readily absorbed. A recent review of early literature relating to magnesium and magnesium alloys used in vivo is available from Witte, Elizer and Cohen (2010). A

comprehensive review of biomaterials based on magnesium alloys is also available from Witte, et al. (2008).

Magnesium materials have shown good biocompatibility and resorbability in animal studies due to their corrosive breakdown into materials the body can process (Yun, Dong et al. 2009, Wang, Shinohara et al. 2009). Magnesium corrodes according to the following reaction:



The above reaction is stepwise broken down into the following reactions:



Magnesium, a necessary element for human metabolism, is found in the body in various concentrations and is efficiently removed by the kidneys through urine (Staiger et al. 2006). Hydrogen gas, a product of this reaction (Equation 3-3), must be absorbed by the body to prevent subcutaneous gas bubbles from forming which may require removal by needle or other means. The ideal implant would degrade over time such that the hydrogen evolution

rate is less than that of the absorption by the body and would maintain structural integrity until the healing process is complete.

Table 3-1 Summary of the physical and mechanical properties of various implant materials in comparison to natural bone - reproduced from (Staiger, Pietak et al. 2006)

Properties	Natural Bone	Magnesium	Ti Alloy	Co-Cr alloy	Stainless Steel
Density (g/cc)	1.8-2.1	1.74-2.0	4.4-4.5	8.3-9.2	7.9-8.1
Elastic Modulus (GPa)	3-20	41-45	110-117	230	189-205
Compressive yield Strength (MPa)	130-180	65-100	758-1117	450-1000	170-310
Fracture Toughness (MPam ^{1/2})	3-6	15-40	44-115	N/A	50-200

The corrosion rate of a wide variety of alloys has been studied *in vitro* (Wang, Estrin et al. 2008, Song 2007, Witte, Fischer et al. 2006, Zhou, Shen et al. 2010, Fekry, El-Sherif 2009, Wen, Wu et al. 2009). *In vitro* testing has been performed using many different testing methods and mediums (Xin, Hu et al. 2010), resulting in a wide range of estimates of corrosion rates. In addition, the actual corrosion rates observed during *in vivo* studies to date differ widely with *in vitro* models, up to 4 orders of magnitude (Witte, Fischer et al. 2006). A significant improvement would be realized if *in vitro* models and processes were developed that more precisely match *in vivo* results.

To lengthen the service life of implants, three basic modifications have been employed: coatings, alloying, and processing to change grain sizes. Coatings have been used to delay the corrosion of the magnesium until the structural integrity of the implant is no longer

required. Various coatings have been employed including high purity magnesium (Salunke, Shanov et al. 2011), stearic acid (Ng, Wong et al. 2010), cerium-based coatings (Ng, Wong et al. 2010), dicalcium phosphate dihydrate (Hu, Wang et al. 2010), anodizing (Song 2007), TiO₂ coatings (Wang, Wang et al. 2009), and various polymers including PCL (Wong, Yeung et al. 2010). The distinct disadvantage of a coating process used to protect the magnesium alloy in this case is that a failure at any point in the coating could result in premature and unpredictable failure of the implant.

Alloying elements with magnesium have long been studied for use in the transportation sector. The use of commercially available magnesium alloys, such as AZ31 with 3 wt% aluminum and 1 wt% zinc, and AZ91, with 9 wt% aluminum and 1 wt% zinc has been considered for implants. The distinct advantage of AZ91 as compared with AZ31 is the reduced rate of hydrogen evolution and implied reduction of corrosion rate. While the hydrogen evolution rate is considered similar to what the human body can tolerate without large gas bubbles forming (Song 2007), the long term effects of the higher concentration of aluminum have not been fully evaluated. Rare earth elements have been added to further reduce the corrosion rate of magnesium alloys with some success (Witte, Fischer et al. 2006), but long term toxicity studies have not yet been performed for these alloys.

Changing the microstructure of metals has been a long standing method of changing mechanical and corrosion properties. It is well known the grain boundaries of metals corrode preferentially as compared to the intra-grain boundary areas, and this well-known phenomenon is the basis for acid etching samples to study metallographically. Several

studies have surfaced which evaluate magnesium alloy corrosion with different processing histories (Wang, Estrin et al. 2008), and the influence of microstructure (Kannan 2010).

To our knowledge, there is no literature which studies the effect of corrosion on the strength of AZ31 magnesium alloy in Hank's solution over the expected life of a load bearing implant. The objective of this research is to quantify the change in mechanical properties of magnesium alloy (AZ31) plates over time submerged in a Hanks Balanced Salt Solution.

Methods and Materials

The materials used to perform the test were purchased off the shelf from a commercial supplier. The testing performed was derived from an ASTM standard test F382-99, *Standard Specification and Test Method for Metallic Bone Plates*. The objective of the testing was to quantify the load capabilities of AZ31 alloy subjected to various immersion durations in a corrosive environment.

Methods

ASTM F382-99 provides terminology and definitions to support bone plate testing which are listed here for completeness:

0.2% Offset Displacement, q (in) – permanent deformation equal to 0.2% of the center loading span distance.

Bending Strength (Lb-in) – the bending moment necessary to produce a 0.2% offset displacement in the bone plate when tested.

Bending Structural Stiffness, EI_e (Lb-in²) – the bone plate’s normalized effective bending stiffness that takes into consideration the effects of the test set-up configuration.

Bending Stiffness, K (Lb/in) – the maximum slope of the linear elastic portion of the load versus load-point curve when tested.

Bone Plate Width, w (in) - the width of the bone plate.

Center Span, a (in) – distance between the two loading rollers.

Fracture Load, F_{max} (Lbs) – the applied load at the time when the bone plate fractures.

Loading Span, h (in) – distance between the loading roller and the nearest support.

Proof Load, P (Lbs) – the applied load at the intersection point of 0.2% offset curve from the Bending Stiffness curve and the observed data.

The Bending Structural Stiffness is determined by the following expression:

$$EI_e = \frac{(2h + 3a)Kh^2}{12} \quad 3-5$$

The center span distance, a , in this test was fixed at 25.4 mm. The support span distance was fixed at 101.6 mm, resulting in the Loading Span, h , of 38.1 mm. Bending Strength is found according to the following:

$$\text{Bending Strength} = \frac{Ph}{2}$$

3-6

The proof load was found by finding the intersection of the 0.2% offset curve and the load versus displacement data obtained from the test. The 0.2% offset curve was found by performing a linear regression on the most linear region of the test data and shifting 0.2% in the abscissa. The linear regression was performed in MATLAB[®] R2009a using a proprietary regression algorithm and choosing an arbitrary minimum number of points of 1000, representing approximately 17.8 newtons and approximately one mm of displacement. To automate the data analysis, a program was written in MATLAB[®] which found the best fit regression with the steepest slope. The linear regression was performed iteratively in ten point increments along the data in order to find the steepest slope region.

To find the proof load, the 0.2% offset curve intersection with the load-displacement data was found. This was performed using MATLAB[®] and automated to avoid personal judgment errors.

Materials

Magnesium alloy (AZ31B-O) in sheet form was chosen as the test material due to its mechanical properties and corrosion potential in the body. The tensile strength of 220 MPa compares favorably to that of human bone, and the addition of aluminum and zinc retards the corrosion process sufficiently to maintain strength during the healing process.

AZ31B-O alloy was procured from Magnesium Elektron N.A. (Madison, Illinois) in sheet sizes of 0.3 meters by 1.22 meters by 3.2 mm thick. The chemical composition was certified to be in accordance with AMS-4375K and QQ-M-44B as per Table 3-2.

Table 3-2 Composition of AZ31 Alloy

	Al	Zn	Mn	Ca	Cu	Fe	Ni	Si	Others (each)	Others (Total)	Magnesium
Min	2.5	0.7	.2	-	-	-	-	-	-	-	-
Max	3.5	1.3	1.0	0.04	0.05	0.005	0.005	0.05	0.1	0.3	Balance

Sample Preparation

Because corrosion is proportional to the surface area exposed to the testing medium, three sample types were prepared: one solid, one with large holes simulating a bone plate, and one with a large number of holes to simulate a mesh structure. The surface areas of the three sample types were calculated using the SolidWorks Computer Aided Design (CAD) software.

Samples for the corrosion test were prepared by cutting the 0.3 meter by 1.22 meter sheets into 160 mm by 19.1 mm (length by width) sizes using a powered sheet metal shear. The shear was fit with a jig to ensure similar sample sizes and all samples were cut at one time.

The samples were then machined using a fixture mounted on a CNC milling center to create consistent sized samples and to remove the high energy edges caused by the shearing process. The samples, six at a time, were loaded into a vise (face to face) such that a sheared

edge was above the vise face. A 25.4 mm diameter insert cutter was then used to cut the edge of the samples to remove the sheared edge. This resulted in one cleanly machined longitudinal edge.

The samples were further machined by placing them in a fixture with the previously machined edge against a pair of reference pins and held in place via clamping pressure of three screws. The bottom piece of the fixture was made from aluminum stock drilled with holes to receive two 6.3 mm pins for alignment and three holes to receive screws to hold in place the top clamping part of the fixture. The top portion of the fixture was made from steel bar stock with the underside machined with a groove to ensure even clamping force on the magnesium samples and prevent samples from moving during the machining process.

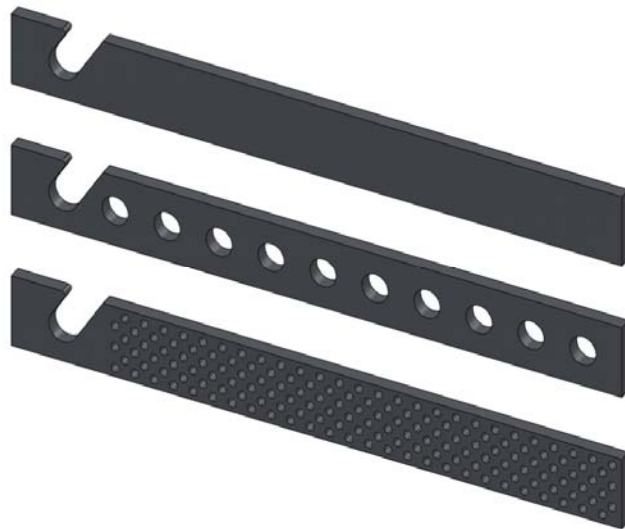


Figure 3-1 Sample configurations: Solid, large holes, and small holes

Samples, two at a time, were loaded into the machining fixture, fitted tightly up against the locating pins in the center, and allowed to protrude past the ends of the clamping fixture (Figure 3-2 and Figure 3-3). A CNC program was written to machine the profile of the samples around the three un-machined edges (thus finishing all four edges, including the first edge that was machined previously) using a 6.3 mm flat end mill. This process ensured a consistent surface finish at the edges of the samples and a consistent size of 15.9 mm wide by 149.2 mm long. The profile of the sample included a slot at the top of the sample to aide in hanging during the testing. The edges were machined square except for the inlet and outlet surfaces of the hook which were given a radius of 1.5 mm to ease assembly of the test rig.



Figure 3-2 Machining fixture in clamped position



Figure 3-3 Machining fixture in open position showing aligning pins

For samples with holes, a hole-drilling routine was added to the program. Large-holed samples were drilled with a 6.3 mm drill bit on the central axis of the sample a total of 10 times, evenly spaced across the face. The small-holed samples were drilled with a 1.88 mm drill bit in a repeat pattern resulting in 156 small holes evenly distributed across the face.

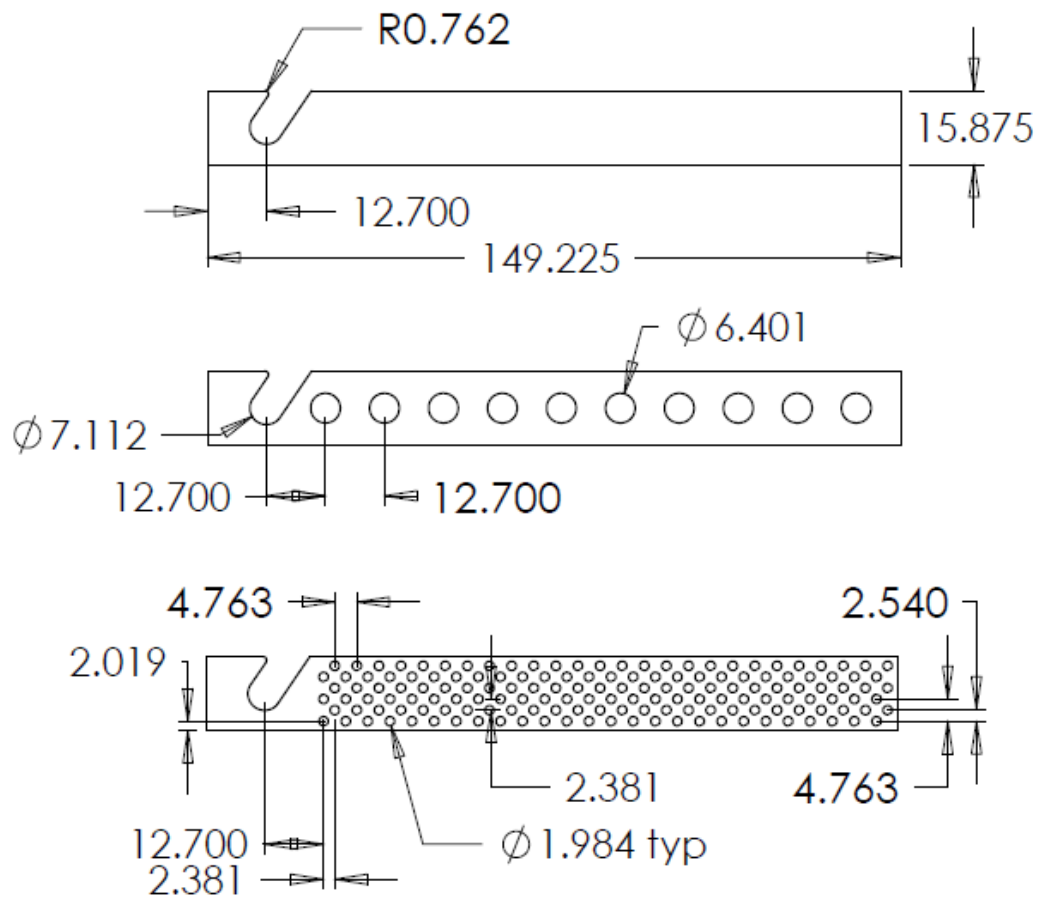


Figure 3-4 Dimensioned drawing of solid plate (top), large-hole plate (middle) and small-hole plate (bottom) (dimensions in mm)

Burrs caused by the machining process were removed using a handheld de-burring tool to avoid injury during assembly of the test rig. The samples were also blown off with compressed air to remove the machining coolant, and stacked on paper towels to further remove moisture introduced during the machining process.

During the machining process, a machining coolant was used to reduce heat build-up on the tool and samples, to flush chips away from the surfaces being machined, and to minimize any fire hazard due to the small magnesium chips and the heat generated from cutting them. The cutting fluid was a water-based coolant and thus caused a dark gray oxide layer to form on the faces of the samples. This was machined away using an abrasive process with 150 grit paper. The surfaces of all of the samples were sanded in a consistent manner until all traces of oxide layer were removed and virgin metal was visible.

The surface area of solid (5665.4 mm^3), small-hole (7729.9 mm^3), and large-hole (5655.1 mm^3) samples were calculated and the samples were then weighed (Table 3-3). These values were recorded, and the samples were immediately hung from their appropriate positions on the test rig. Sample statistics were calculated and are presented in Table 3-4 along with the original surface area.

Table 3-3 Initial sample masses (grams)

Week	Solid (g)			Small hole (g)			Large Hole (g)		
	Sample #			Sample #			Sample #		
	1	2	3	1	2	3	1	2	3
0	12.678	12.764	12.771	9.942	9.870	9.950	10.979	10.931	10.940
2	12.770	12.765	12.753	9.834	9.868	10.007	10.950	10.910	10.923
4	12.716	12.744	12.763	9.889	9.910	9.951	10.959	11.001	10.948
6	12.715	12.698	12.810	9.928	9.880	9.885	10.991	10.964	10.932
8	12.757	12.712	12.718	9.849	9.978	9.894	10.899	10.940	10.933
10	12.739	12.712	12.744	9.969	9.968	9.999	10.937	10.975	10.945
12	12.724	12.689	12.720	9.816	9.936	9.919	10.954	10.928	10.904
14	12.814	12.769	12.793	9.913	9.898	9.977	10.914	10.880	10.920
16	12.721	12.783	12.678	9.994	9.892	9.988	10.929	10.954	10.935
18	12.696	12.748	12.787	9.895	9.962	10.015	10.850	10.950	10.953
20	12.806	12.723	12.799	9.939	9.904	9.958	10.880	10.919	10.957

Table 3-4 Sample statistics, mass data in grams

	Solid	Small Hole	Large Hole
Theoretical Mass (g)	12.784	9.998	10.980
Mean Mass (g)	12.746	9.927	10.934
SD	0.038	0.053	0.032
Max	12.814	10.015	11.001
Min	12.678	9.816	10.850
Range	0.136	0.199	0.151

Test Rig Preparation

The test rig consisted of a tower constructed of extruded aluminum sections. The vertical section held a motorized linear slide to allow vertical translation of the samples during the test. The test rig was assembled using off-the-shelf materials, including a 24 volt DC gear motor and several custom-made connectors from the motor to the test platform.

The samples were moved vertically in their individual tanks of Hanks Solution at a frequency of 2 cycles per minute. Each cycle resulted in the sample being moved up 6.3 mm from the bottom position and then back down to the bottom position.

The test rig allowed the sample platform to be raised approximately 254 mm to allow access to the individual containers of Hanks Solution for maintenance. The test platform slid on a box slide vertically such that the solution level for each sample could be monitored and adjusted accordingly.

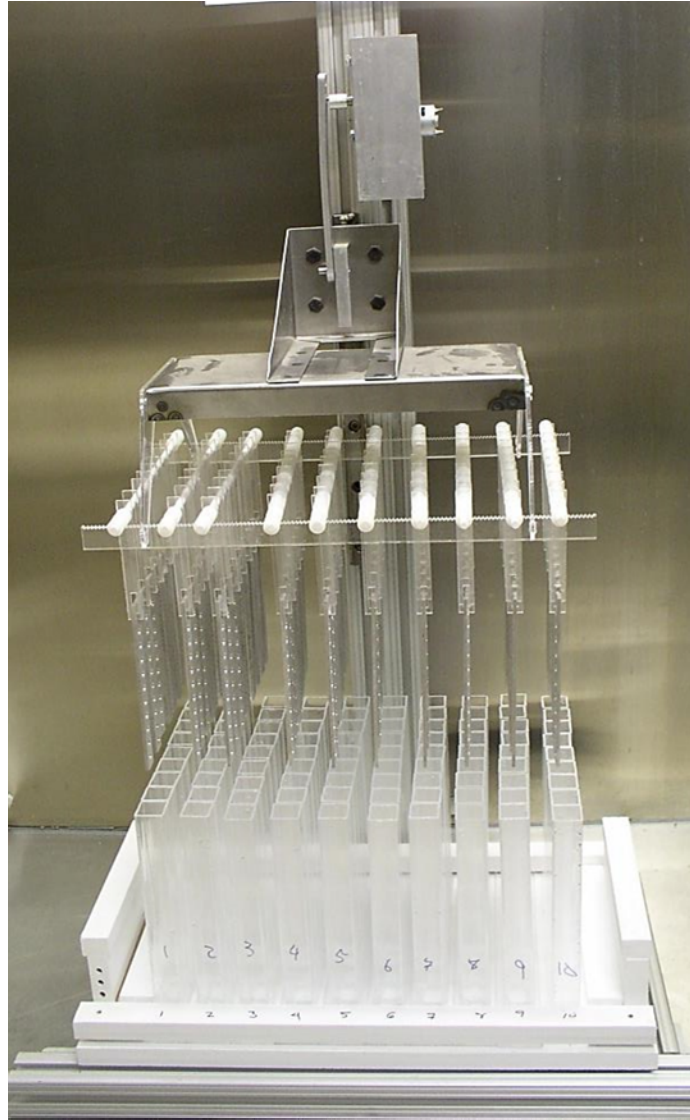


Figure 3-5 Test rig configuration showing samples hanging over empty test containers

The test platform was made from sheet steel bent and spot welded for rigidity. A hanging system was built from an acrylic sheet to allow adjustment of position from front to back of the test containers. The hanging system was bolted to the test platform and used 6.3 mm fiberglass rods running front to back with nine individual hangers on each rod for the test

samples. Ten rods were placed on the hanging system to allow for a total of 90 sample locations (ten rods with nine sample locations on each rod). Each rod contained three solid samples, three large-hole samples, and three small-hole samples. This represented the number of samples to be tested at each testing interval.

Testing containers were devised and constructed using an acrylic sheet and extruded acrylic square tubing. The square tubing was cut into lengths of 203 mm, and the parts were de-burred and cleaned in preparation for assembly. A base of 6.3 mm thick acrylic sheet was cut to 38.1 mm width and 279.4 mm length. Each row of nine cut extruded tubes was then attached to the acrylic sheet using adhesive, creating a series of containers capable of holding approximately 100 mL of fluid each. The containers measured approximately 25.4 mm by 25.4 mm (outside) by 203 mm high. The nine individual containers represent the number of samples to be tested at each testing interval.

Hanks Balanced Salt Solution (HBSS) was purchased from HyClone (Logan, Utah) and mixed according to instructions except that distilled water was used in lieu of de-ionized water. The pH of the Hanks solution was adjusted as instructed to a level of 7.4. Each sample container was filled with 90 mL of the mixed HBSS, and the containers and samples were housed in a computer-controlled environmental chamber (Figure 3-6) which was electronically programmed to maintain the human body temperature of 37° C for the duration of the test.



Figure 3-6 Environmental chamber used to maintain temperature conditions

Samples were immersed in the sample containers (Figure 3-7) for the duration of the test except during maintenance of the test solution when the samples were briefly raised up for the refreshing of the test solution.

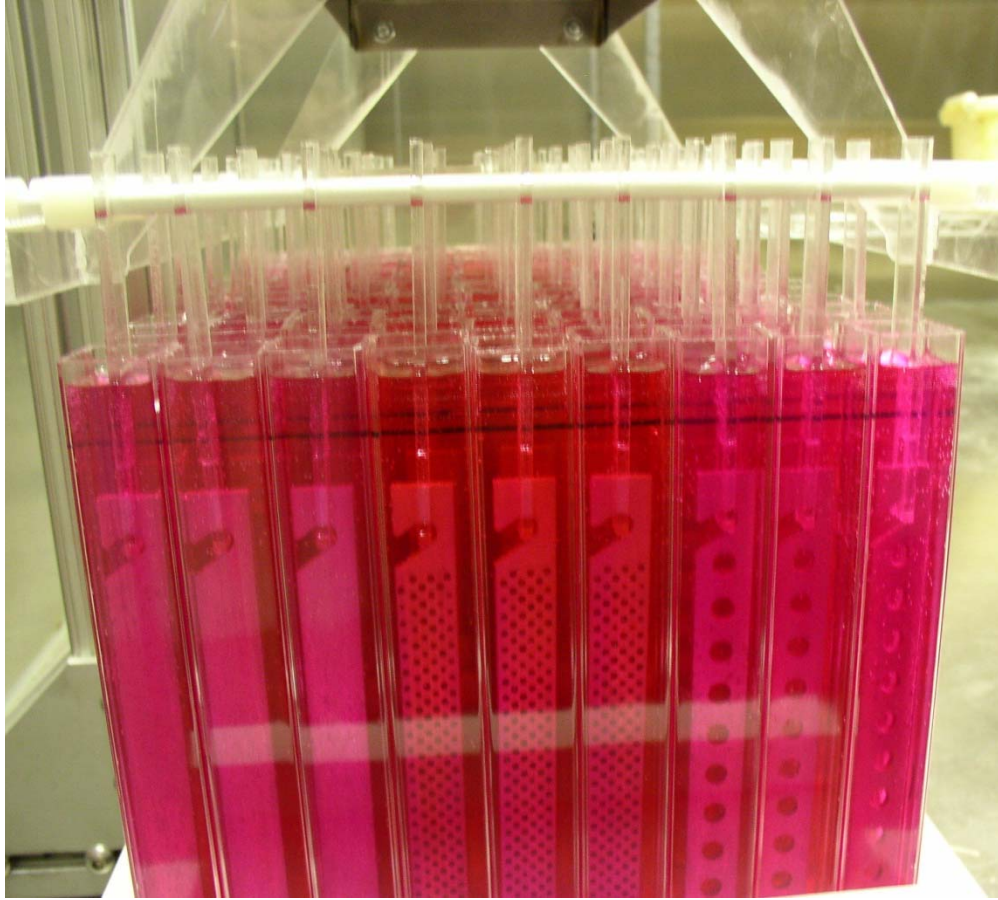


Figure 3-7 Test apparatus and samples immediately after start of test

Maintenance of the test solution was done three times per week - Monday morning at 8:00 AM, Tuesday afternoon at 5:00 PM, and Friday at noon. During the initial filling of the solution in each test container, the 90 mL level was marked. At maintenance times, distilled water was added to the original mark to replace water that had evaporated. The pH of the distilled makeup water was adjusted to a pH of 7.4 by adding NaOH or HCL. Approximately 10 to 12 mL of water evaporated during the Tuesday to Friday interval (the longest interval between refilling) from each sample container, and approximately 8 to 10 mL evaporated

during the Friday to Monday interval. The Monday to Tuesday interval showed the least evaporation.

At testing intervals of two weeks, the Hanks solution was removed from each test container, and the test container was rinsed with water. Each container was then refilled with fresh Hanks Solution. One set of nine test specimens was removed for testing, and the remaining samples were again submerged in the test solution.

Sample Testing

At each two week interval, one rod with nine samples was removed, and samples were prepared by immersion in a distilled water bath for one minute followed by immersion in ethyl alcohol for two minutes. The samples were then air dried in the environmental chamber (Figure 3-8). The mass of each sample was measured and recorded, and an image was taken for a visual record of corrosion progress.

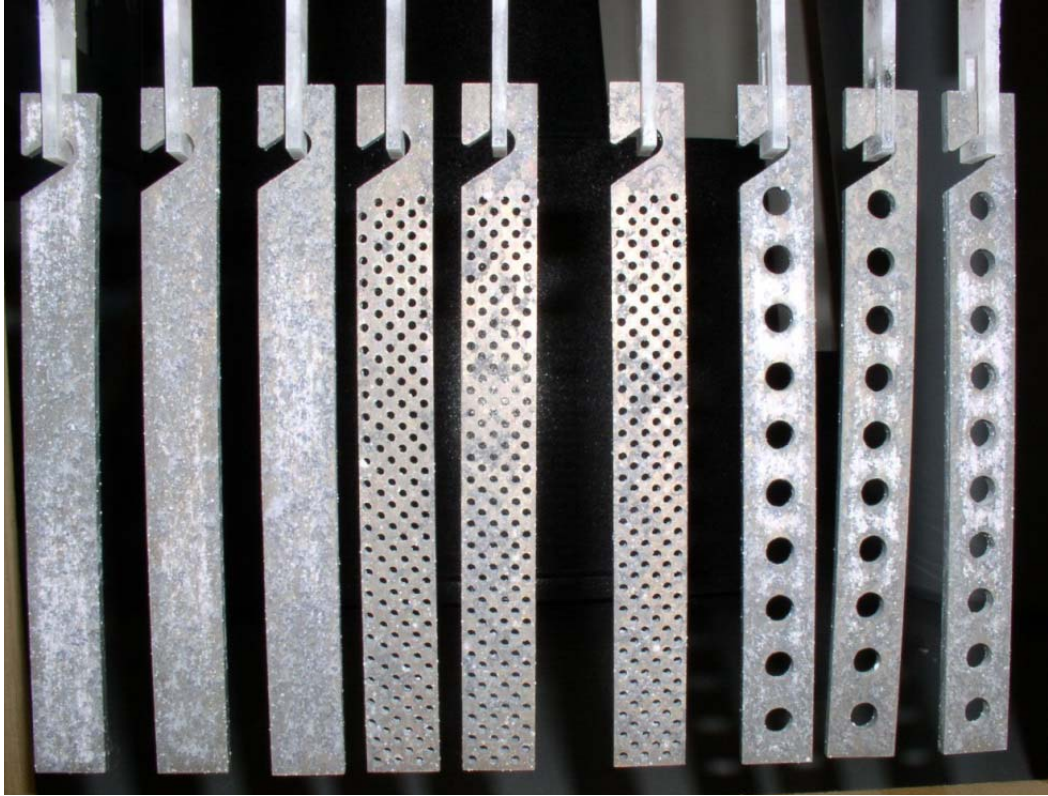


Figure 3-8 Test samples drying in environmental chamber following corrosion test and testing preparation

The samples were then subjected to a 4 point bend test on an Applied Test Systems 1620C universal testing machine, in accordance with ASTM F382-99 (Standard Specification and Test Method for Metallic Bone Plates). The large span for the four point bend test was selected to be 101.6 mm to correspond to the distance between the first and last holes on the large-hole samples. In accordance with ASTM F382-99, the small span included two holes resulting in a small span width of 25.4 mm (Figure 3-9 and Figure 3-10). To ensure consistency between samples, a fixture was created to align the samples on the test rig in the same position and orientation for every test. The rate of loading was specified as 2.54 mm per minute and was continuous for 10.2 mm at which point the direction was

reversed and the unload rate was increased to 5.08 mm per minute. The load versus displacement data were recorded for each sample and retained for evaluation.

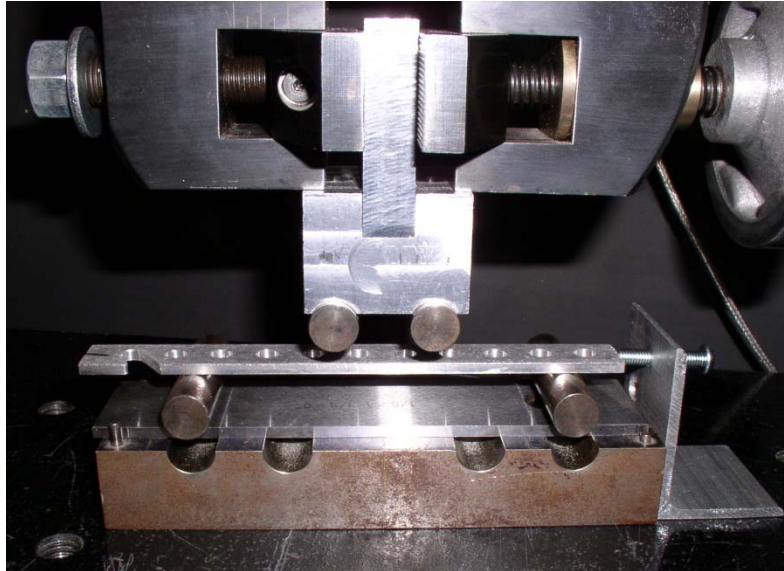


Figure 3-9 ASTM F382-99 test set up with large span of 101.6 mm and small span of 25.4 mm

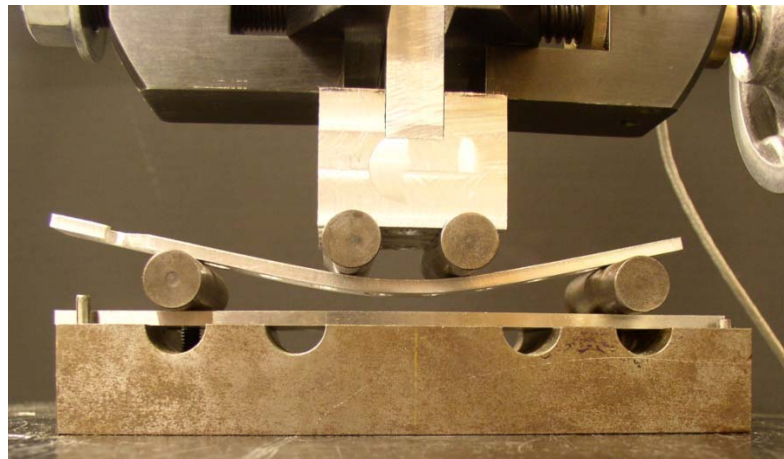


Figure 3-10 ASTM F382-99 bending test during loading

Results

The bending strength (Figure 3-11) showed generally decreasing trends over time as expected due to corrosion. Bending strength for samples with no holes decreased from an average of 2.37 N-m to approximately 2.19 N-m over the 20 week test, however this was not statistically significant ($t(4) = 1.48, p > 0.05$). The no-hole samples retained approximately 92% of their original bending strength. The large-hole sample average bending strength decreased from 1.88 N-m to 1.43 Nm, retaining approximately 76% of the original bending strength ($t(4) = 3.50, p < 0.05$ (two-tailed)). Small-hole samples average bending strength decreased from 1.61 N-m to 1.26 N-m over the same 20 week test, retaining approximately 78% of the original bending strength ($t(4) = 11.73, p < 0.05$ (two-tailed)).

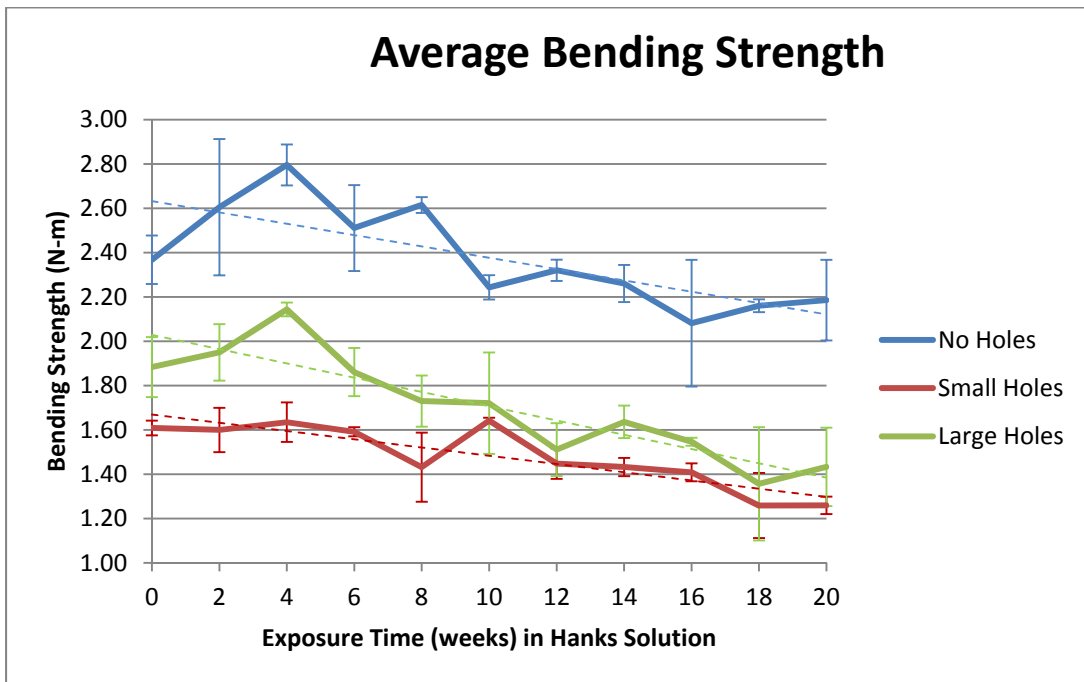


Figure 3-11 The average 0.2% offset proof load of samples versus time (Error bars are Standard Error)

The average bending stiffness (Figure 3-12) for no-hole samples decreased from 90,800 N/m to 78,057 N/m, retaining approximately 86% of the stiffness over the measurement period ($t(4) = 5.19$, $p < 0.05$ (two-tailed)). Large-hole sample stiffness decreased from 65,376 N/m to 48,830 N/m, retaining approximately 75% of the stiffness ($t(4) = 3.39$, $p < 0.05$ (two-tailed)), and small-hole sample stiffness decreased from 42,086 N/m to 30,232 N/m, retaining approximately 72% of the original stiffness ($t(4) = 11.16$, $p < 0.05$ (two-tailed)).

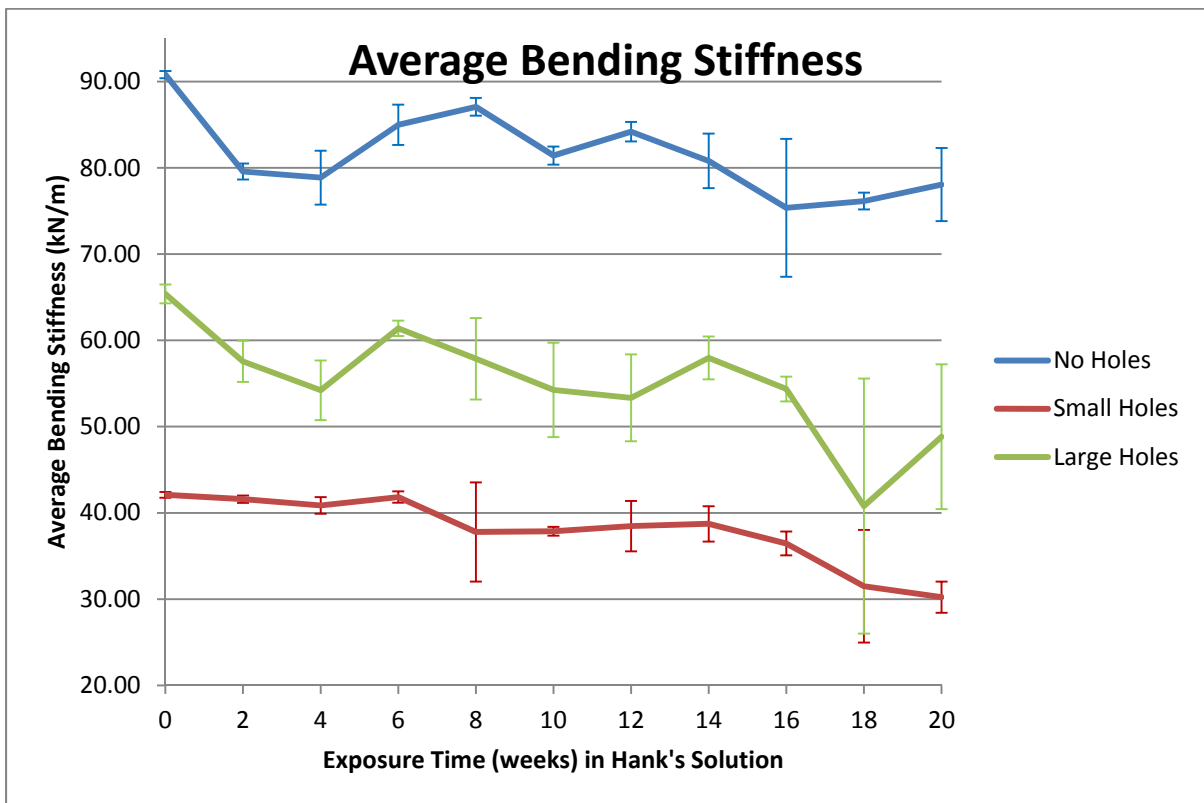


Figure 3-12 Average Bending Stiffness of samples versus time (Error bars are Standard Error)

The mass of the samples (Figure 3-13) as measured after immersion, rinsing and drying overnight showed generally increasing trends over time. The mass increased due to the accumulation of corrosion products on the surface of the samples. The decrease in proof load and average bending stiffness as well as the increase in mass are as expected.

Differences in mass gain for solid samples versus small-hole samples were only significant at week two ($t(4) = 6.825$, $p < 0.05$ (two-tailed)), meaning solid samples gained more mass at week 2 as compared to small-hole samples. Differences in mass gain for solid samples versus large-hole samples were significant only at week 12 ($t(4) = -2.974$, $p < 0.05$ (two-tailed)), meaning large hole samples gained more mass than solid samples at this time period. All other comparison within time periods were not significant at $p < 0.05$ confidence levels.

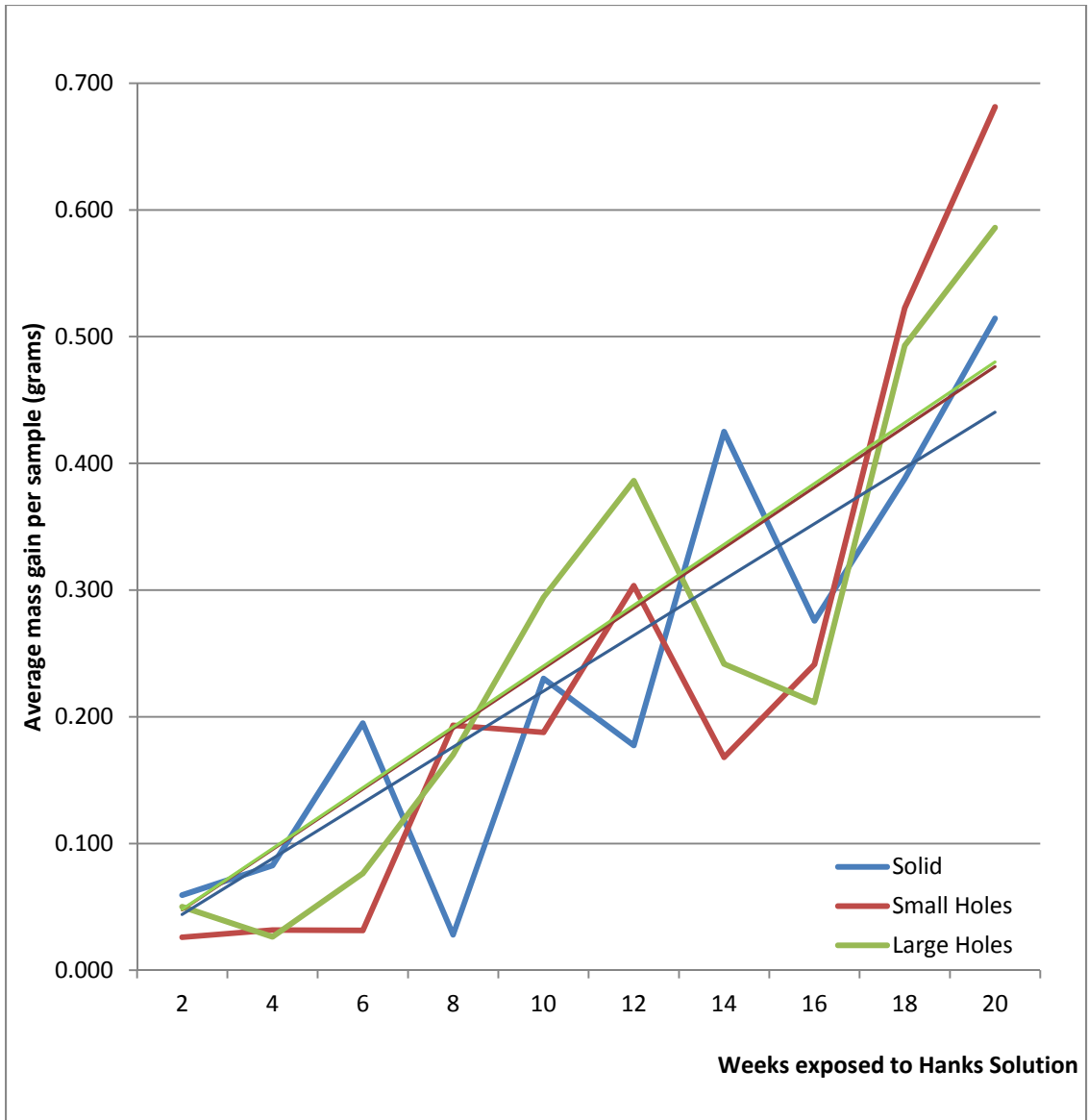


Figure 3-13 Average mass gain versus time, in grams, including linear trend line

Table 3-5 Final sample masses, in grams

Week	Solid (g)			Small hole (g)			Large Hole (g)		
	Sample #			Sample #			Sample #		
	1	2	3	1	2	3	1	2	3
0	12.678	12.764	12.771	9.942	9.870	9.950	10.979	10.931	10.940
2	12.827	12.817	12.822	9.854	9.899	10.034	11.022	10.942	10.969
4	12.864	12.793	12.814	9.890	9.941	10.014	10.962	11.077	10.948
6	12.811	12.852	13.145	9.978	9.928	9.881	11.144	11.026	10.946
8	12.782	12.788	12.701	9.933	10.025	10.343	10.914	11.357	11.011
10	12.770	13.109	13.007	10.155	10.174	10.170	11.073	11.158	11.509
12	12.864	12.770	13.031	10.405	10.088	10.088	11.313	11.242	11.390
14	13.041	13.262	13.348	10.000	9.996	10.296	11.449	10.862	11.128
16	12.757	12.929	13.323	10.254	10.165	10.179	11.128	11.156	11.168
18	13.150	13.149	13.096	10.691	10.415	10.334	10.835	11.444	11.953
20	13.562	13.551	12.758	10.646	10.599	10.600	10.832	11.984	11.698

Table 3-6 Sample mass gain in grams with average

Week	Solid (g)			Avg (g)	Small hole (g)			Avg (g)	Large Hole (g)			Avg (g)
	Sample #				Sample #				Sample #			
	1	2	3		1	2	3		1	2	3	
0	0.000	0.000	0.000	0.000	0.000	0.000	0.000	0.000	0.000	0.000	0.000	0.000
2	0.057	0.052	0.069	0.059	0.020	0.031	0.027	0.026	0.072	0.032	0.046	0.050
4	0.148	0.049	0.051	0.083	0.001	0.031	0.063	0.032	0.003	0.076	0.000	0.026
6	0.096	0.154	0.335	0.195	0.050	0.048	-0.004	0.031	0.153	0.062	0.014	0.076
8	0.025	0.076	-0.017	0.028	0.084	0.047	0.449	0.193	0.015	0.417	0.078	0.170
10	0.031	0.397	0.263	0.230	0.186	0.206	0.171	0.188	0.136	0.183	0.564	0.294
12	0.140	0.081	0.311	0.177	0.589	0.152	0.169	0.303	0.359	0.314	0.486	0.386
14	0.227	0.493	0.555	0.425	0.087	0.098	0.319	0.168	0.535	-0.018	0.208	0.242
16	0.036	0.146	0.645	0.276	0.260	0.273	0.191	0.241	0.199	0.202	0.233	0.211
18	0.454	0.401	0.309	0.388	0.796	0.453	0.319	0.523	-0.015	0.494	1.000	0.493
20	0.756	0.828	-0.041	0.514	0.707	0.695	0.642	0.681	-0.048	1.065	0.741	0.586

Discussion

The nine samples collected in week four showed generally uniform corrosion with some evidence of pitting corrosion. Samples collected in week six showed generally uniform corrosion over the entire exposed surface. Pitting corrosion was evident in week six, but had not become a major source of corrosion products on the surface. In week eight, large scale corrosion products had accumulated on two of the nine samples - one with large holes and one with small holes. The corrosion accumulation was approximately 10 mm in diameter and 6 mm in thickness. The surrounding areas of the magnesium were heavily corroded and showed considerable pitting corrosion.

Samples evaluated after week eight generally showed results similar to those of week eight. Of note, several test specimens exhibited very little corrosion, even after 18 or 20 weeks in HBSS. This can be attributed to several factors, including the inherent variability in the corrosion process, the corrosion mechanism (primarily pitting corrosion) which is driven by metal association with chloride ions, and the micro-galvanic corrosion process which is dependent on differential of galvanic activity between the grain boundaries and the grains themselves.

During testing, it was observed that corrosion products on the surface of the samples caused a significant variation in the test specimen-test rig interaction. The corrosion products were significantly more brittle than the bulk material and the load versus displacement curve would show an initial spike in load followed by a period of constant load, due to load points and support points located on corrosion products. As the corrosion

products broke down, the load would then continue to increase. To eliminate these artificial affects, corrosion products at the points of support fixture and loading fixture interfaces with the test specimen were removed after week six testing. The corrosion products were removed using a mechanical scraping action with a steel blade.

Overall a gradual reduction in bending stiffness and bending strength can be attributed to increasing corrosion penetration over time. Considering the consolidation time for long bone fractures in children is 5 to 25 weeks (Berger, De Graaf et al. 2005) with a mean of 12 weeks, the bending strength retention between 76% and 92% measured in this study suggests AZ31 magnesium alloy could be a good candidate as a resorbable fixation material for orthopedic applications.

Related and Further Work

Further work needs to consider the effects of limiting access of the fluid to only 3 sides of the test specimen as if it were a bone plate attached to the bone, to modify the test conditions to more accurately reflect the in vivo conditions, to evaluate coatings on the magnesium alloy to tune degradation rate, and to evaluate the addition of elements and coatings to improve bone growth (hydroxyapatite, etc) and retard corrosion. Improvements in the test conditions to consider include larger pH buffering capabilities, fluid media flowing over and around the samples being tested (instead of static solution), and mechanical loading to simulate the activity that an implant is expected to endure during the healing process. An additional problem to consider is how to eliminate, limit or remove gas pockets caused by the corrosion of the metal implant. In this study, small gas bubbles were visually observed on the samples

in the first week of testing, when there was not an observable corrosion layer to obscure visual observation.

While the AZ31 alloy shows relatively slow degradation in strength over time in Hanks Balanced Salt Solution in this test, applications for load bearing fixation would be subject to variable loading over the course of healing. Future work should consider loading effects on strength retention and corrosion rate. Other corrosion mechanisms (other than galvanic, micro galvanic and general corrosion) may affect the corrosion rate and strength retention, and should be considered. Other corrosion mechanisms worthy of consideration include Stress Corrosion Cracking (SCC) and fatigue corrosion just to mention two.

Conclusion

The bending strength and stiffness results show a slow decrease over time rather than an abrupt decrease. Solid plate segments retained approximately 92% of their strength, while small-hole and large-hole samples retained approximately 78 and 76% of their initial bending strength over the 20 week immersion corrosion test. This slow decrease in strength would provide adequate time for the bone to heal and would slowly transfer load carrying from the implant to the bone. This research suggests that AZ31 may be a reasonable material for orthopedic biodegradable implants.

4. MECHANICAL PROPERTIES ANALYSIS OF AZ31 MAGNESIUM ALLOY UNDER DIFFERENT LOADING CONDITIONS IN HANKS BALANCED SALT SOLUTION

^aRonald L. Aman, ^bOla L. A. Harrysson, ^cDenis Marcellin-Little, ^dDenis R. Cormier, ^eHarvey A. West, ^fC. Thomas Culbreth

^a NC State University, ron_aman@ncsu.edu

^b Associate Professor, Dept. of Industrial and System Engineering, NC State University. harrysson@ncsu.edu

^c Professor, Orthopedic Surgery, College of Veterinary Medicine, NC State University. denis_marcellin@ncsu.edu

^d Professor, Department of Industrial and Systems Engineering, Rochester Institute of Technology. drceie@rit.edu

^e Research Assistant Professor, Dept. of Industrial and System Engineering, NC State University. hawest@ncsu.edu

^f Professor, Dept. of Industrial and System Engineering, NC State University. culbreth@ncsu.edu

Introduction

The service life of an implant is important to consider when designing a custom implant for reconstruction and fixation. Load bearing biodegradable metallic implants have special considerations in this light, since they are designed to degrade over time, and thus the functionality is intentionally reduced by corrosion. Understanding corrosion rates in the various conditions which the implant is expected to perform is important to reduce risk of premature failure in place, and to avoid excess exposure to degrading implant materials.

Evaluation of corrosion rates has been performed *in vitro* in various mediums (including Hank's Balanced Salt Solution, Simulated Body Fluid (SBF), sodium chloride solution, and others) using several methods. Potentiodynamic polarization and electrochemical impedance spectroscopy are popular test methods which evaluate the potential for corrosion and can

estimate corrosion current density. These test methods can provide estimates of corrosion rate in a short period of time by accurately measuring potential and electron flow. While the data can be collected easily, interpretation is complex.

Simple immersion tests evaluate the corrosion rate by leaving the test specimen in a container with testing medium for some time. These tests take longer and require maintenance of test conditions over long periods of time; however, the corrosion rates can be more meaningfully interpreted.

Corrosion rate plays an important role in determining the expected life of a bio-degradable implant, however other factors such as fatigue life and static stresses may play a large role as well (Song, Atrens 2004). Corrosion fatigue life is likely to be shorter than both corrosion life and the fatigue life due to interaction of both corrosion and fatigue (Nan, Ishihara et al. 2008, Kang, Yao et al. 2009), yet little information is available about this phenomenon with magnesium alloys.

This study examines the mechanical strength degradation of simulated bone plates and screws made from magnesium alloy AZ31 in an environment simulating *in vivo* conditions. Each bone plate is attached to two artificial bone segments simulating orthopedic open reduction internal fixation. Groups of samples are subjected to three different loading conditions while being immersed in a corrosive environment, one cyclic, one static, and one with no load applied for reference. The cyclic loaded samples are meant to evaluate the corrosion fatigue performance of AZ31, while the statically loaded samples evaluate the stress corrosion cracking performance of AZ31. Samples are subjected to eight different lengths of exposure to simulated body fluid, from two to twenty weeks. The bending

strength of each sample is measured and compared across groups to characterize the mechanical performance.

Materials and Methods

For this study AZ31H-24 was chosen as the test material. The magnesium alloy AZ91D was excluded from this study since it has approximately three times the aluminum in the alloy as compared to AZ31. Aluminum has been measured in tissue (2.1-4.8 $\mu\text{g/L}$ in blood serum) (Tahan, Granadillo et al. 1994) indicating the tolerance of some aluminum, however there has been at least one study linking it as a risk factor for Alzheimer's disease (Miu, Benga 2006).

Simulated bone plates using AZ31 alloy were manufactured in consistent form and size using computer controlled machining centers. The bone plates were cut from a single rolled sheet with the long direction in the direction of the axial grains developed in the rolling process. The sheet was mechanically sheared with a 3.2 mm machining allowance on the edges of the bone plates. The bone plates were then CNC drilled for precise screw positions using high speed steel drills. The plates were anchored to a fixture for further processing using these screw holes. They were positioned accurately using two pins and machined using carbide milling cutters to the final size. A round-over bit was used to remove sharp edges on the top and bottom surfaces of the plate (Figure 4-1).



Figure 4-1 Simulated bone plate model

The plates were then de-burred mechanically using a file, tumbled in ceramic media for 100 hours and rinsed with alcohol prior to weighing. Cortical bone screws were fabricated from the same alloy procured from Magnesium Elektron N.A. (Madison, Illinois) in extruded bar form measuring 6.3 mm by 2 meters. The bar was machined to screw form by Dynamic Machining and Manufacturing (157 Industrial Drive, King, NC). The screws were machined on a Citizen L-20 Type VIII Computer Numerical Control (CNC) Swiss style screw machine using a whirling head. The screws were rinsed with alcohol, and allowed to air dry prior to weighing (Figure 4-2). The screws were not subjected to ceramic media tumbling to avoid deformation of the delicate screw threads.



Figure 4-2 Bone screw model based on a 3.5 mm cortical bone screw

Simulated bone segments were fabricated from polyacetal Delrin[®] using CNC milling centers. Flat surfaces were machined on opposite sides of the hollow cylinder bone segments to accommodate the flat bone plate. Holes were drilled and tapped to accept the bone screws, and grooves were added to the bottom transversely to aid in locating the constructs in the containers on cylindrical supports.

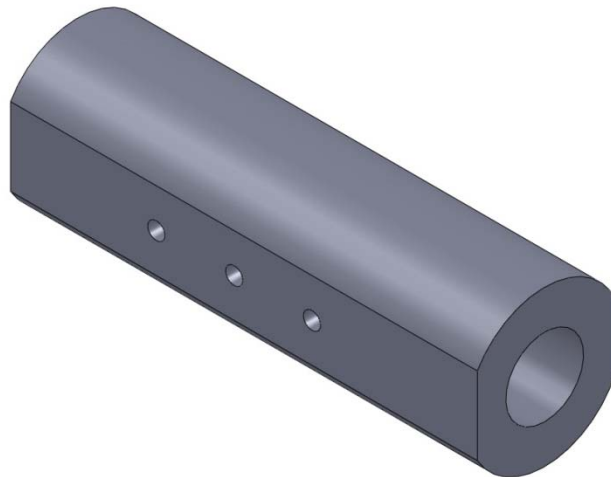


Figure 4-3 Simulated bone segments fabricated from Delrin

The constructs were assembled after weighing the bone plate alone and the bone plate and six screws together (Figure 4-4 and Figure 4-5). The screw running torque was measured with a torque wrench to be approximately 0.06 N-m. Screws were driven by hand to a point near the interface of the head and the bone plate, and then torqued using a calibrated torque wrench to 0.73 N-m.

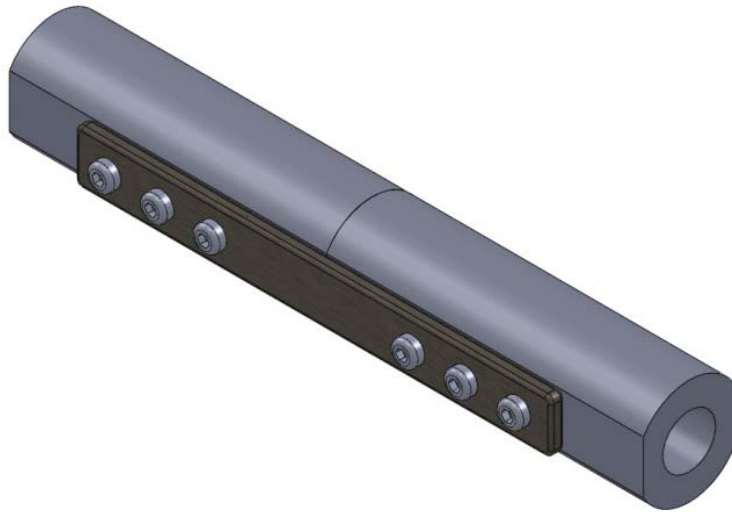


Figure 4-4 Model of assembled bone construct

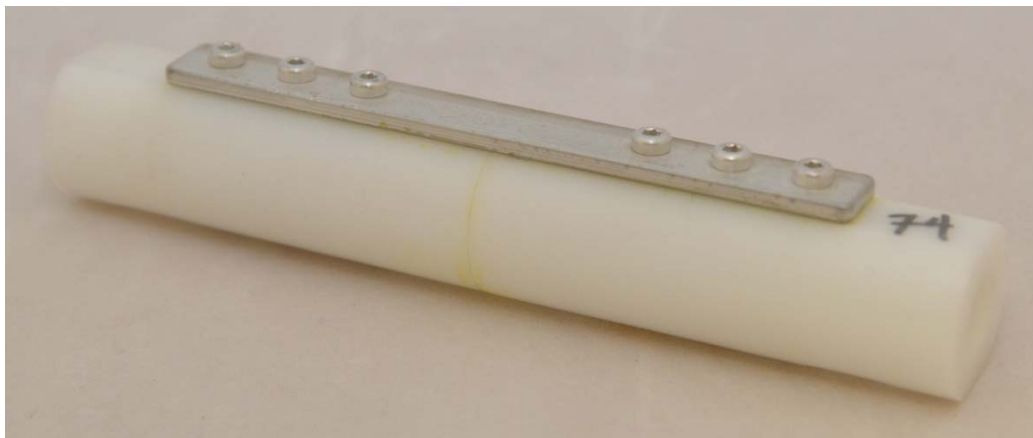


Figure 4-5 Assembled bone construct

Separately, five bone screws were tested to evaluate the torque characteristics of the custom magnesium alloy screws. The hex drive socket heads of four screws stripped out at approximately 0.8, 0.9, 0.9 and 1.1 N-m respectively, and one screw broke near the thread run-out at approximately 1.2 N-m. It was determined for the purpose of this test that 0.7 N-m was an acceptable torque.

The test apparatus consisted of an upper tank (Figure 4-6) that held 4 rows of 15 individual containers, one each for each test specimen undergoing testing during that particular interval. Two supply lines (for uniformity) charged from a circulating pump maintained the tank full, and the level was regulated by an overflow drain to a heater tank located below. The test media was circulated to improve temperature uniformity and to simulate *in vivo* fluid flow conditions. Individual containers had a fluid inlet cut out at the top edge adjacent to the long channels in the tank. Drains provided limited flow of approximately 5 mL per minute through the individual containers simulating limited fluid flow in the body (Knothe Tate 2003). The total liquid volume (volume of Hanks solution used per test interval) was 30 liters, and makeup water was added once per week to maintain the fluid level in the heater tank. A level gage mounted to the outside indicated water level, and the initial level was marked at the outset of the test. Temperatures were monitored on a regular basis in the individual containers to verify 37 ± 0.5 °C for the duration of the test.

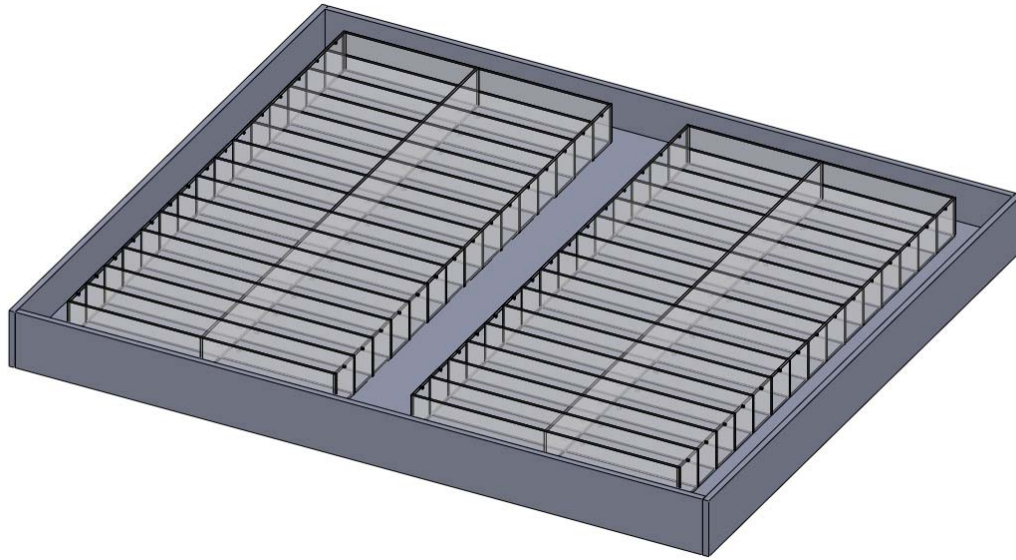


Figure 4-6 Model of test platform showing four test rows with containers for 15 samples

Three different test conditions were evaluated as follows. A total of 15 test specimens were evaluated at each interval, five each exposed to different load conditions comprised of non-loaded, statically-loaded and cyclically-loaded specimens. Loads were applied using two separate but similar carriages (Figure 4-7) attached to a frame around the test platform. Each carriage contained 20 hollow aluminum cylinders with internal springs applying a load to Delrin rods which transferred the load axially down to Delrin loading blocks. The Delrin load transfer rods were machined identically with one end flat and the opposite end with a radius to keep the load centered on the loading blocks. A cross hole was machined through the cylinders and load transfer rods to receive a holding pin which allowed the Delrin loading rods, along with the springs, to be held in place and out of the way during maintenance periods (Figure 4-8).

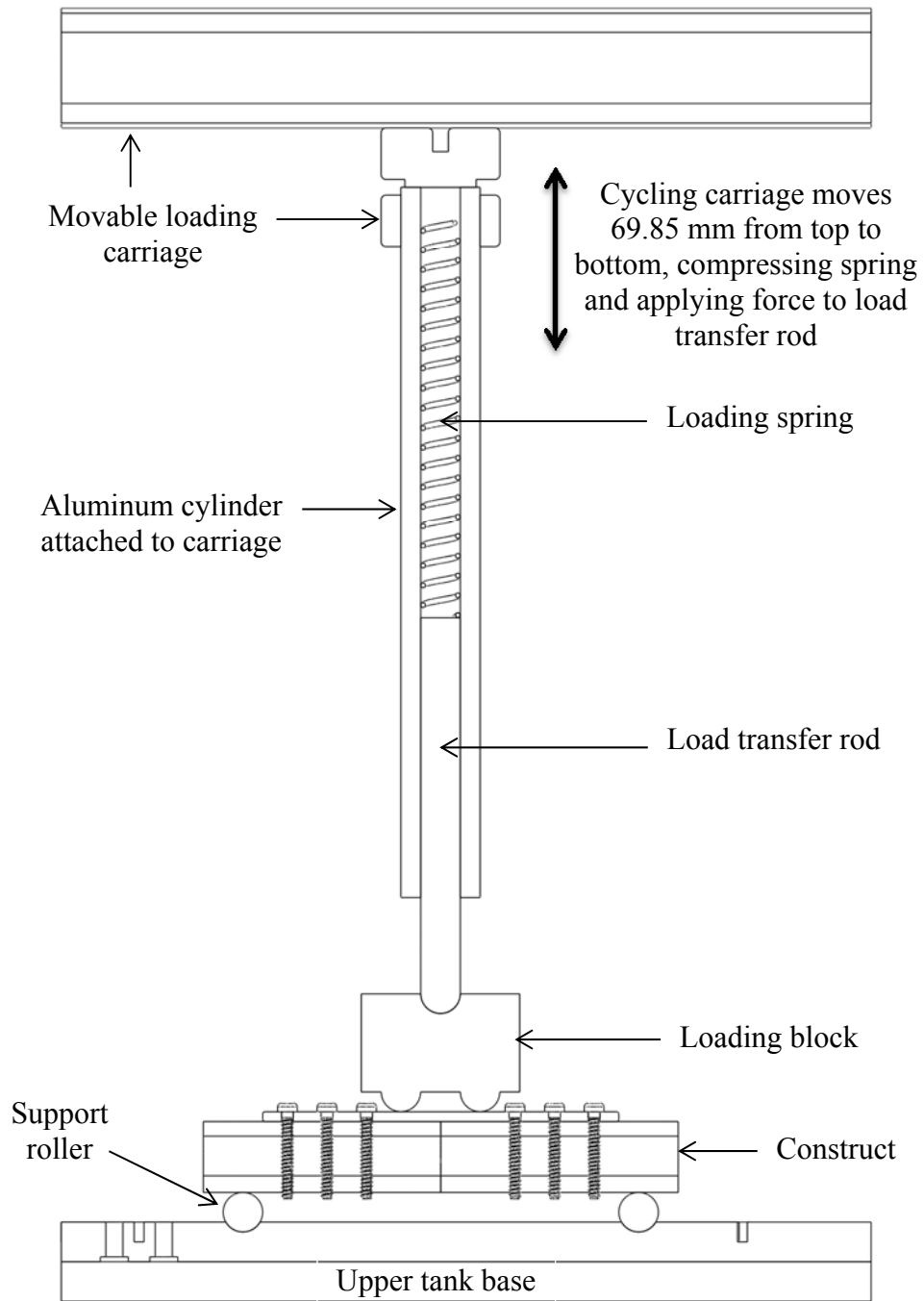


Figure 4-7 Schematic of testing apparatus with construct in place

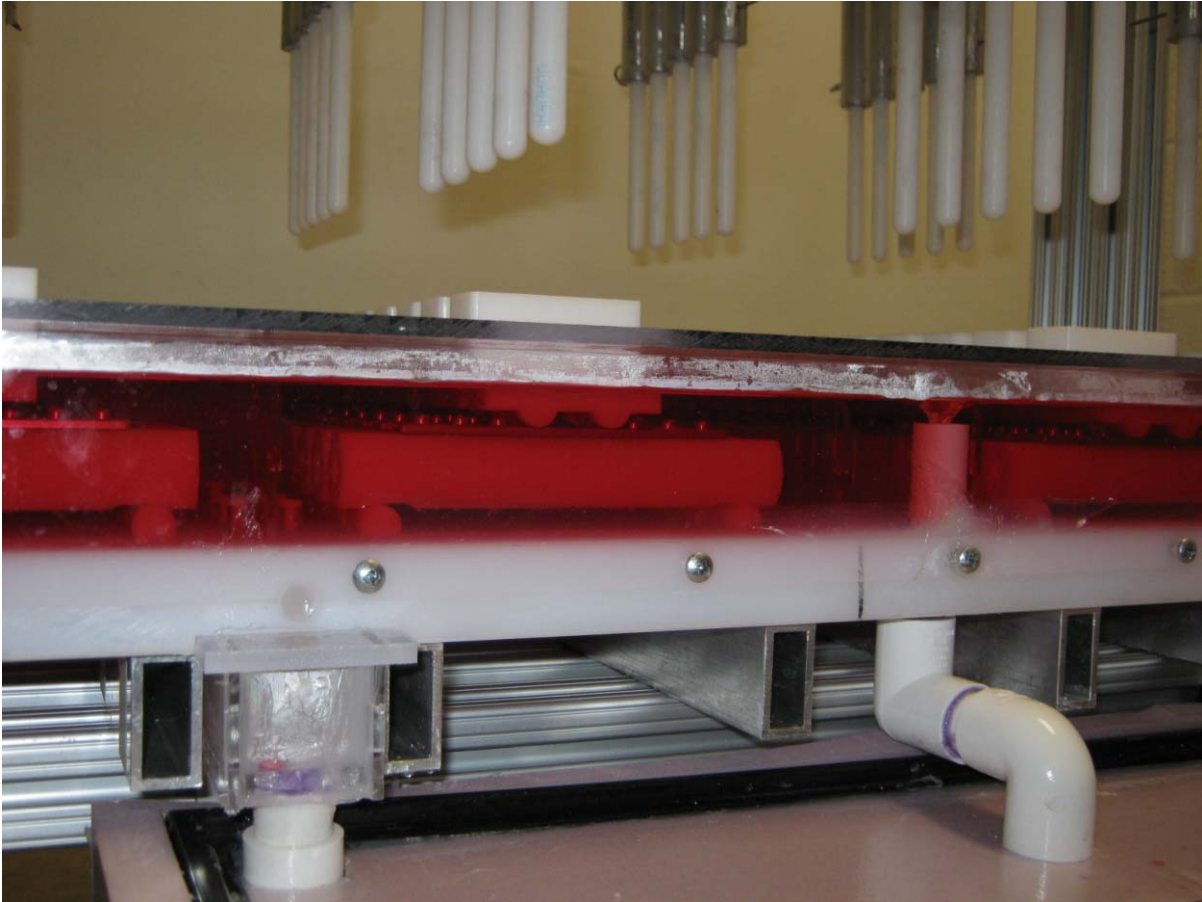


Figure 4-8 Test rig immediately prior to initiation of loading. Note the aluminum cylinders (background top), Delrin loading rods with radius end showing, loading blocks, and constructs. HBSS with phenol red is easily seen, along with level-controlling overflow

Cyclic loading was accomplished by moving the loading carriage vertically from the top position down 69.85 mm using a DC motor, chain and sprocket, and a rotary to linear linkage. The system was geared to achieve the necessary 712 N force required for applying 20 individual 35.6 N loads. A voltage regulator was used to control the speed of the DC motor to achieve a loading/unloading cycle time of 24 seconds.

Static loading was accomplished by manually moving the loading carriage from the fully retracted position to the loading position. The loading position was equivalent in height to

the bottom of the loading cycle in the cycling loading set up. Reference screws were used to mark the loading position and to prevent over loading during the loading cycle. The carriage was held in the loading position by screws.

The loading blocks were machined to receive two 12.7 mm cylinders (Delrin) spaced 25.4 mm apart on the bottom which transferred the axial load from the loading rods onto the bone construct below it (Figure 4-7 and Figure 4-8). The top of the loading blocks were machined with a hemisphere to receive the radiused end of the loading rods (Figure 4-9). An acrylic sheet was machined to accurately position and orient the loading plates and to minimize the evaporation of the HBSS in the upper tank. The loading blocks were also machined with radiused edges to minimize interference with the acrylic alignment cover and to maximize the cover's ability to seal the upper tank. Loading blocks were placed on every construct (including non-loaded samples) to maintain consistency.

To reduce heat loss, foam insulation was put in place around the sides and on top of the upper testing tank, as well as around and on top of the lower heater tank. The insulation was fitted to reduce heat loss and to limit evaporation of HBSS, but was not to interfere with operation of the loading rods (Figure 4-10).



Figure 4-9 Top view of upper tank of test rig. Note the loading blocks with hemi-sphere machined in top and the acrylic aligning the loading blocks (numbers are written on acrylic to denote chamber position, not sample identification)



Figure 4-10 Assembled and operating testing rig. Note: dynamic loading is in the foreground, static loading in the background and no-load samples were in the middle

One set of 15 test specimens was removed from the Hank's Balanced Salt Solution (HBSS) every two weeks up to a maximum of 20 weeks, except for weeks 12 and 18. The temperature of the solution in the individual containers (Figure 4-6) was maintained at 37 ± 0.5 °C for the duration of the test except during the biweekly draining, cleaning and recharging of the HBSS. Temperature control was maintained by a programmable temperature controller utilizing Proportional-Integral-Differential (PID) control, which monitored the temperature in the upper testing tank. A 1500 W water heater element with a voltage regulator was used as the heat source. This was done to reduce the high intensity localized heating of the fluid in the lower tank and to increase the longevity of the heating element in the corrosive environment.

The base of the upper tank was made from polyethylene and was machined to receive acrylic sheets to separate the individual containers. To create consistent test conditions, two identical test regions were constructed. Each test region consisted of two back-to-back rows of 15 individual containers. This was done to ensure linear flow of HBSS from the upper test tank (which surrounded the two test regions) across the test constructs and down through a drain – nearest the center of the test region (Figure 4-11). Each of the individual containers was identical in volume and contained a single fluid make-up hole located in the short-side wall at the opposite end of the individual containers from the drain.

The base of the upper tank was machined to receive 12.7 mm diameter Delrin rods spaced 101.6 mm apart in each of the individual containers. This provided the lower support for the constructs. These supports were elevated to allow for dynamic and static loading to deform the construct without interference up to 10.2 mm.

The upper tank was enclosed on the sides using acrylic sheeting machined to size and attached using screws to the polyethylene base. The sides and bottom were sealed with a silicone sealant to prevent leaks.

The drains from each of the individual containers in a test region emptied into a common drain which returned to the lower heater tank. The drains were sized and tested to allow approximately 5 mL of fluid flow through each of the individual containers per minute to simulate fluid flow *in vivo*.



Figure 4-11 Testing apparatus view from above showing individual testing locations, orificed drains (center) and makeup water inlets at the sides. Note the corrosion on the samples to the right (after 2 weeks) as compared to the newly inserted 8-week samples

Cyclic loading was performed at a rate of 2.5 cycles per minute which would subject the 20 week test samples to 500,000 cycles. The cyclic loading was accomplished using a DC

motor driven mechanism linked to the samples, as described above, via springs, where the spring constant was determined such that the displacement of the drive mechanism to deflection of specimen ratio was 100. Springs were tuned via elongation and cutting to produce a load of 35.1 ± 0.45 N at maximum displacement. Cyclic testing was performed in accordance with a modified version of ASTM F382-99 and ASTM F2502-11.

The loading force was determined by first identifying the bending strength for a construct in accordance with ASTM F382-99. The static and dynamic loading force was then specified to be one quarter of the bending strength to ensure that a majority of the cyclic loaded samples would survive the testing period, and would be available for bending strength testing.

The static loading was performed by imparting a constant load on the top surface of the specimens, in a similar fashion to the cyclic loading set up, and as described above. Springs were tuned in the same manner as above resulting in a loading of 35.1 ± 0.45 N at maximum displacement.

After specimens were subjected to the test regimen for the specified period of time, they were removed from the HBSS, thoroughly rinsed with distilled water, rinsed with ethanol and left to air dry. Constructs were stored in tightly sealed plastic bags until all of the samples were subjected to HBSS for their specified term.

Corrosion products were removed using chromic acid etching, consisting of 200g of anhydrous chromic acid crystals (CrO_3) and 19g silver nitrate (AgNO_3) with 1L of deionized water. Samples were immersed in the chromic acid solution for 15 minutes under an acid

hood. Samples were then removed from the acid solution and thoroughly rinsed with deionized water. Samples were then air dried and rinsed a third time with ethanol.

Samples were allowed to air dry for several weeks. Mass readings were taken at regular intervals until sample masses reached equilibrium as defined by consecutive mass readings taken at daily subsequent intervals differing by less than 0.5 mg. A subset of samples was scanned using micro-computed tomography for later use.

Mechanical testing of constructs was performed according to ASTM F382-99, using a 4 point bend testing configuration (Figure 4-12, Figure 4-13 and Figure 4-14). The samples were placed on an ATS universal testing machine fitted with a support fixture with major spacing of 127 mm. The crosshead was fitted with a loading head centered on the major span with the minor span of 25.4 mm and the distance between support and loading points of 50.8 mm. A preload of 0.45 to 2.2 N was applied at the initiation of the test.

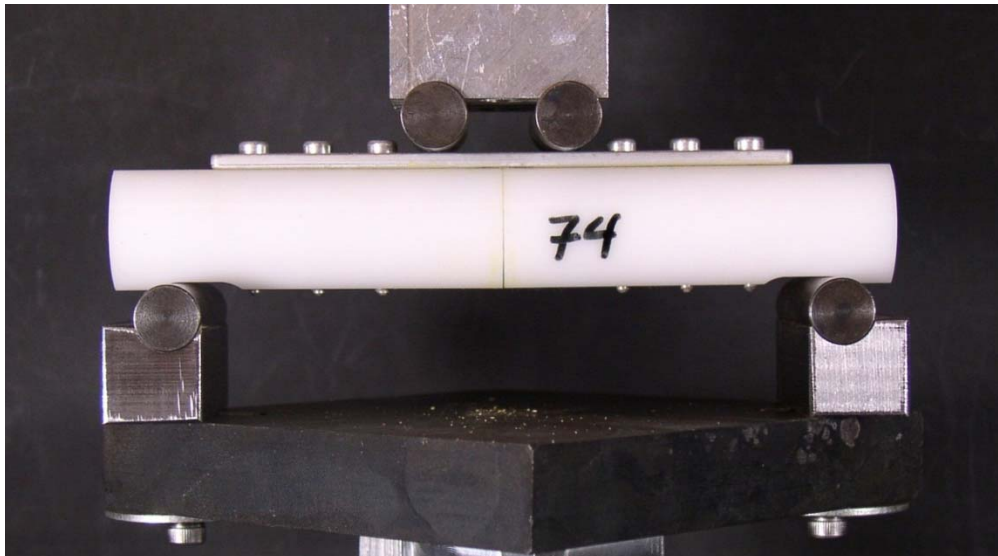


Figure 4-12 ASTM F382-99 testing set up on universal test machine

Crosshead advancement speed was set to 2.54 mm per minute. The stopping condition was fracture, where measured load was 50% of maximum load, or a maximum crosshead displacement of 10.2 mm was reached. Maximum crosshead displacement was chosen to avoid interference of the construct's outside screws with the support fixture as the construct deflected under load. Load and displacement data were collected via the universal test machine for each specimen.

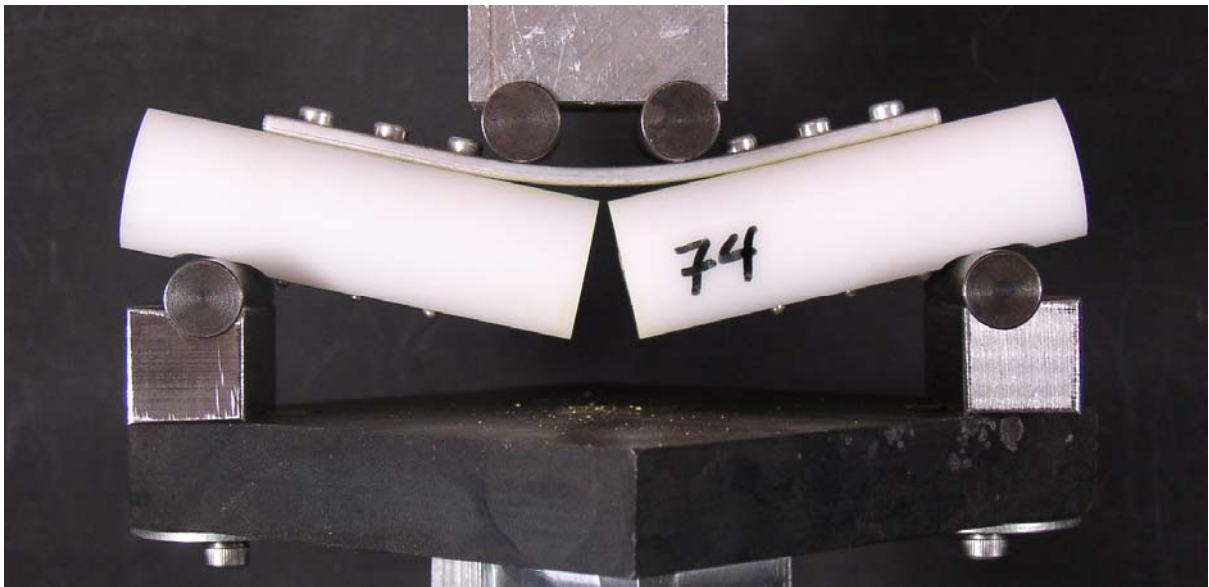


Figure 4-13 ASTM F382-99 4 point bend test at full displacement of a non-corroded sample

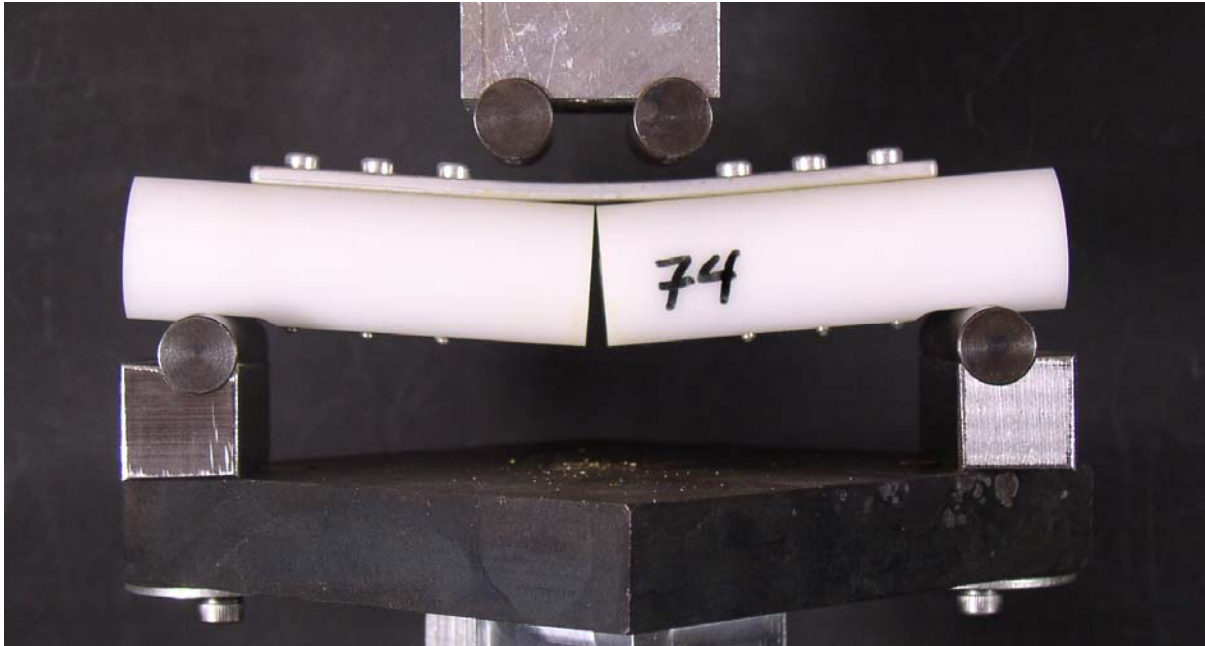


Figure 4-14 ASTM F382-99 4-point bend test showing permanent plastic deformation of a non-corroded sample. Crosshead returned to initiation location (Figure 4-12)

Results

Average mass loss per week per specimen over all specimens was 0.101 mg/week with a standard deviation of 0.02 mg/week. Mass loss per week broken down by loading and time periods is shown in Table 4-1. There was no effect on mass loss for loading $t(78) = 0.45$ $p > 0.05$ (two-tailed) between cyclic loading and non-loaded, and $t(78) = 0.04$ $p > 0.05$ (two tailed) for static loading and non-loaded samples.

Table 4-1 Mass loss (grams) per week for cyclic loaded (CY), non-loaded (NL) and static loaded (ST) specimens

Week	CY	NL	ST	Average
2	0.1296	0.1206	0.1090	0.1198
4	0.1105	0.1081	0.1063	0.1083
6	0.0914	0.1120	0.1045	0.1026
8	0.1101	0.1165	0.1035	0.1100
10	0.0751	0.0747	0.0881	0.0793
14	0.0826	0.0748	0.0832	0.0802
16	0.1029	0.0893	0.0968	0.0963
20	0.1145	0.1030	0.1087	0.1087
Average	0.1021	0.0999	0.1000	0.1007
SD	0.017	0.017	0.009	
CV	0.164989	0.17018	0.09106	

Comparisons of time period effects on mass loss are summarized in Table 4-2. For a one-tail test, the data are significant for $t_{0.1,14} \geq 1.345$.

Table 4-2 Time period comparisons of weekly average mass loss given in *t* statistic values (14 df)

	2 vs.						
4	1.619	4 vs.					
6	2.318	0.866	6 vs.				
8	1.587	-0.344	-1.350	8 vs.			
10	6.221	5.258	3.951	7.293	10 vs.		
14	6.371	5.440	4.024	7.951	-0.195	14 vs.	
16	3.593	2.162	1.064	3.229	-3.567	-3.698	16 vs.
20	1.700	-0.080	-1.037	0.311	-6.231	1.700	-2.612

Bending strength averages are presented in Table 4-3 (including all samples, with the assumption that the bending strength = 0 for samples that broke in the corrosion tank) and

Table 4-4 (including all samples except those that broke in the corrosion tank). Figure 4-15 and Figure 4-16 show graphical results of Table 4-3 and Table 4-4 respectively.

Table 4-3 Bending strength averages (N-m) for all samples, including those that broke during corrosion process

		Mean	SD	CV
2	CY	3.08	0.19	0.06
	NL	3.33	0.26	0.08
	ST	3.28	0.08	0.02
4	CY	2.77	0.30	0.11
	NL	2.98	0.17	0.06
	ST	3.01	0.06	0.02
6	CY	2.39	0.27	0.11
	NL	2.92	0.17	0.06
	ST	2.84	0.07	0.03
8	CY	2.07	0.29	0.14
	NL	2.71	0.15	0.06
	ST	2.75	0.18	0.06
10	CY	1.85	0.26	0.14
	NL	3.00	0.27	0.09
	ST	2.59	0.32	0.12
14	CY	1.21	0.24	0.20
	NL	2.73	0.26	0.10
	ST	2.35	0.41	0.17
16	CY	0.37	N/A	N/A
	NL	2.37	0.25	0.11
	ST	1.86	0.22	0.12
20	CY	0.00	N/A	N/A
	NL	1.81	0.24	0.13
	ST	1.33	0.28	0.21
	Ref	3.73	0.14	0.04

Table 4-4 Bending strength averages (N-m) for all samples except those that broke during corrosion process

		Mean	SD	CV
2	CY	3.08	0.19	0.06
	NL	3.33	0.26	0.08
	ST	3.28	0.08	0.02
4	CY	2.77	0.30	0.11
	NL	2.98	0.17	0.06
	ST	3.01	0.06	0.02
6	CY	2.39	0.27	0.11
	NL	2.92	0.17	0.06
	ST	2.84	0.07	0.03
8	CY	2.07	0.29	0.14
	NL	2.71	0.15	0.06
	ST	2.75	0.18	0.06
10	CY	2.31	0.26	0.11
	NL	3.00	0.27	0.09
	ST	2.59	0.32	0.12
14	CY	2.02	0.24	0.12
	NL	2.73	0.26	0.10
	ST	2.35	0.41	0.17
16	CY	1.85	0.00	0.00
	NL	2.37	0.25	0.11
	ST	1.86	0.22	0.12
20	CY	0.00	0.00	N/A
	NL	1.81	0.24	0.13
	ST	1.33	0.28	0.21
	Ref	3.73	0.14	0.04

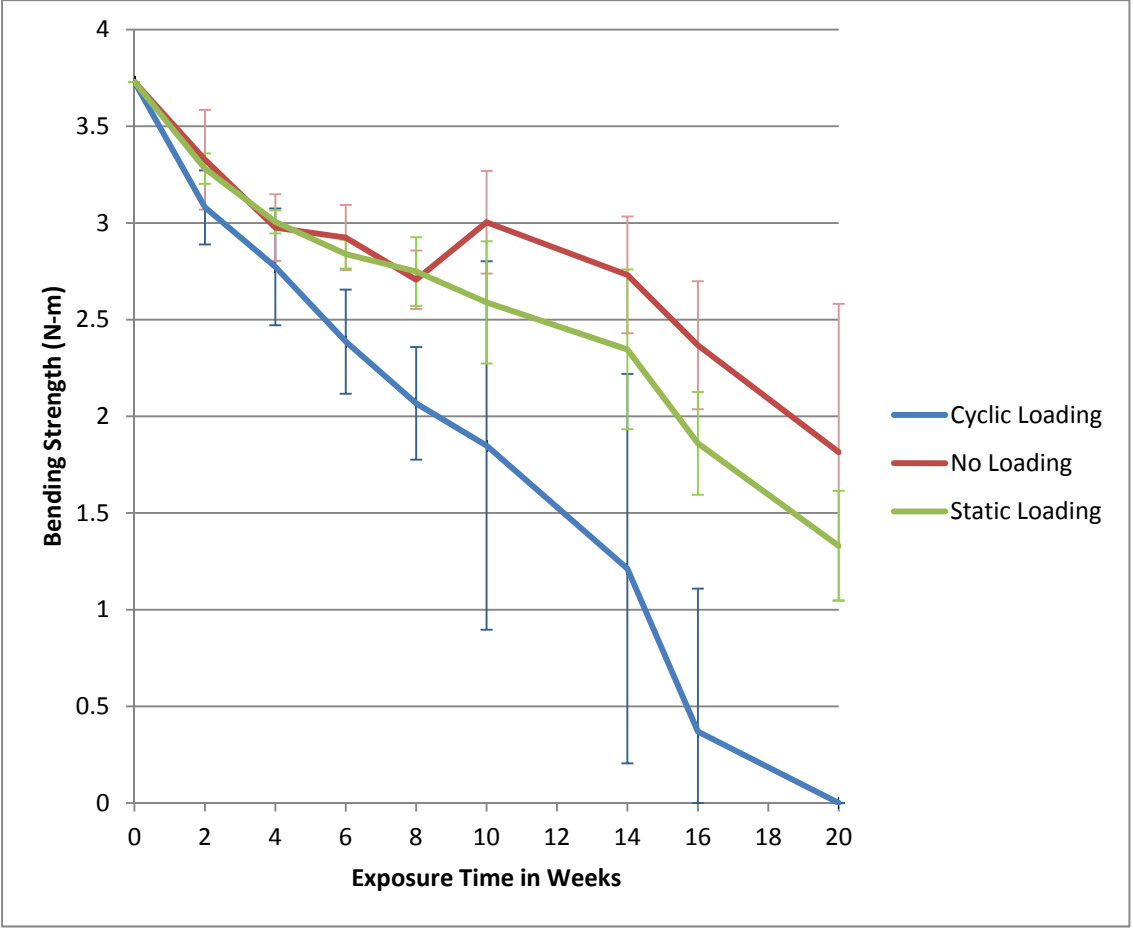


Figure 4-15 Average bending strength vs. exposure time in weeks. Samples broken during corrosion process assumed to have bending strength of 0 (Error bars are Standard Error)

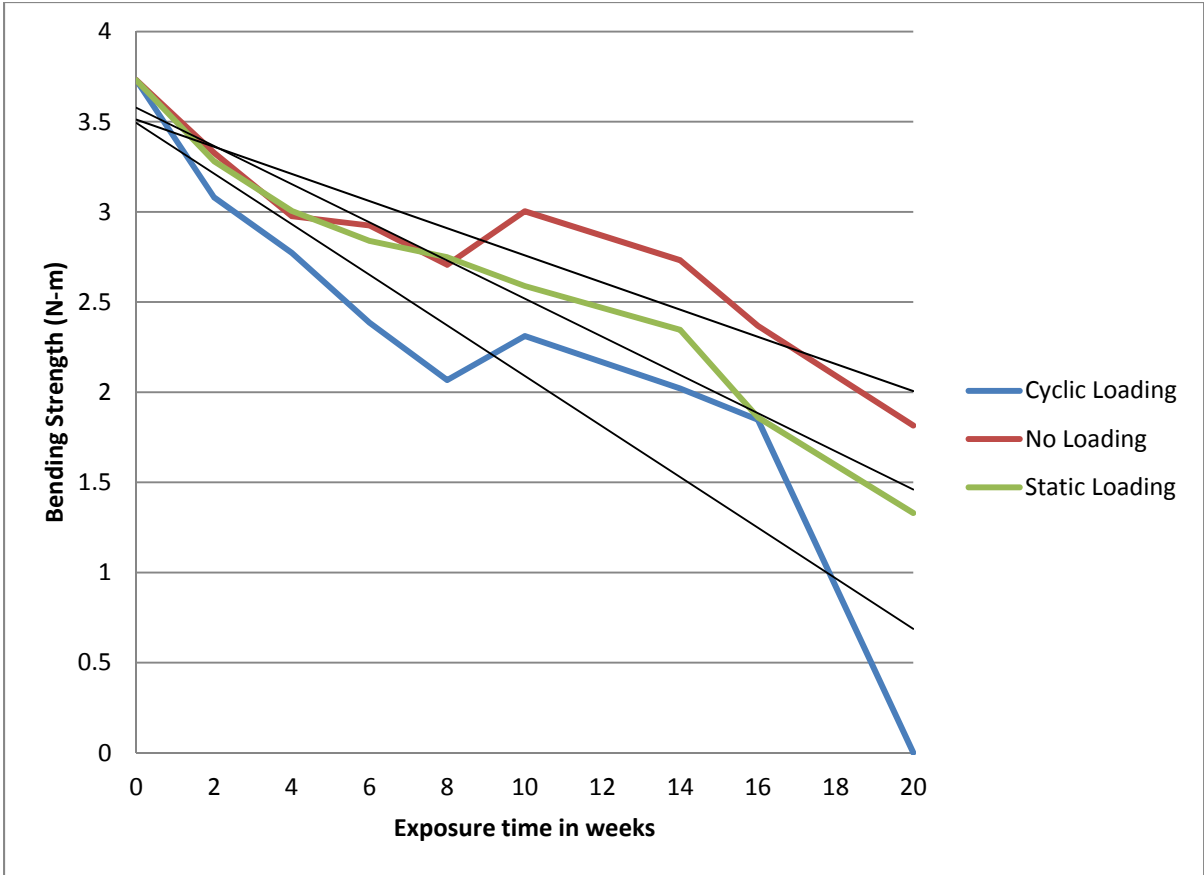


Figure 4-16 Average bending strength vs. exposure time in weeks. Samples broken during corrosion process are not included

Discussion

Corrosion rates as measured by mass loss are notoriously variable. In this case, measured mass loss does not differ significantly among loading groups (cyclic versus non versus statically loaded samples). Corrosion rates compared between time periods show significant differences between all time periods and the two week samples at the 90% confidence level. The week 2 samples showed the highest rate of mass loss averaged over the two week period.

The week 8 samples showed the second highest rate of mass loss, followed by the week 20, 4, 6, 16, 14, and 10.

Of interest is comparing the strength retention of constructs within time periods, that is – does loading have a significant impact on the load carrying capacity of an implant? In this case, assuming a 90% confidence threshold, the significant differences can be found between the cyclic and the statically loaded samples in all weeks (2, 4, 6, 8, 10, 14, 16, and 20). Statically loaded samples retained their strength over the course of the test better than the cyclically loaded samples. Comparing cyclically loaded samples to non-loaded samples over the same time periods and with the same threshold reveals no difference in the time periods 2 and 4, but significant difference in the strength retention in periods 6, 8, 10, 14, 16, and 20. Non-loaded samples retain more of their load carrying capacity over time as expected. Comparing non-loaded samples to statically loaded samples is less conclusive; weeks 2, 6 and 8 are not statistically different, whereas weeks 10, 14, 16, and 20 showed better load carrying performance for non-loaded samples. In week 4, the statically loaded samples showed better load retaining capabilities than non-loaded samples. This interesting result switches over weeks 6 and 8 (which were not significant) to the non-loaded samples performing better in week 10 and beyond. In this analysis, samples that failed in the corrosion tank were not included except for week 20 samples, all of which had failed. The data in Table 4-4 reflect the removal of the samples that failed.

Comparison of the reference samples that were not subject to corrosion to those subject to corrosion revealed significant reductions in bending strength across all samples. Simply

subjecting samples to a corrosive environment has an impact on bending strength regardless of loading.

Based on this analysis, understanding the *in vivo* conditions to which the implant will be subjected is important for the design. Implants subjected to repeated stresses over the life of the implant will need to have a larger cross section area of inertia to overcome reduced load carrying capacities caused by fatigue, even when the loads are 25% of the original bending stiffness.

A total of 12 samples failed (fractured) in the corrosion tank. These samples were maintained in the corrosive environment until the next cleanout period, where they were removed and replaced by a placeholder of similar displacement and height. The first sample to fail (sample number 46) was replaced by sample 126 which then remained in the sample pool for 12 weeks. These data were excluded from bending strength analysis because it was a single data point with no comparison data, but was included in the mass loss calculations. Samples that failed were maintained in the corrosive environment until the next scheduled cleanout, thus when calculating mass loss per week the time immersed was used, not the time to failure.

Only cyclically loaded samples fractured in the corrosion tank. The shortest period to fracture was 56 days (sample 46). The average days of exposure prior to fracture was approximately 81.7 days with a standard deviation of approximately 16.4 days. One cyclic sample remained unbroken at the conclusion of the test in the 16 week samples, and 3 remained unbroken in the 14 week test. The single 12 week sample discussed above remained unbroken, as well as 4 of the 10 week samples.

Figure 4-15 and Figure 4-16 show two interpretations of the bending strength data. Figure 4-16 shows the calculated bending strength determined by 4-point bend testing excluding any zero data (samples that failed during the corrosion process) except that from week 20. Of note are the standard deviations used to determine significance, where the number of data points is variable (excluding those that were 0). With only one sample remaining in the cyclic loaded group from week 16, no standard deviation exists, and similarly the available data points for weeks 14 and 10 were reduced by the number of broken samples. This could have an impact on the true nature of the differences between groups and should be considered carefully.

In vitro studies have been notoriously variable and have not translated well to *in vivo* results. Much more work needs to be done to evaluate if the conditions used in this study represent those experienced *in vivo*. Animal studies need to be constructed with sufficient size to reduce the variance such that meaningful conclusions can be drawn. In the future, better and more reliable *in vitro* corrosion testing processes need to be developed to reduce development costs of potential implant materials. However little is actually known about the corrosion mechanism and physiological responses to corrosion *in vivo*. Future work should focus on developing a good understanding of these phenomena, and translating that to a meaningful *in vitro* corrosion test.

Conclusion

In this work, it was shown that a significant difference exists in the load carrying capabilities of implants over time based on whether the implant is subjected to loads, either

cyclic or static in nature. The loads chosen in this work were relatively modest at 25% of the original bending strength, yet they reduced the effective implant life by a significant amount.

5. MODELING CORROSION OF AZ31 FOR OPTIMIZING CUSTOM OPEN REDUCTION INTERNAL FIXATION

^aRonald L. Aman, ^bOla L. A. Harrysson, ^cDenis Marcellin-Little, ^dDenis R. Cormier, ^eHarvey A. West, ^fC. Thomas Culbreth

^a NC State University, ron_aman@ncsu.edu

^b Associate Professor, Dept. of Industrial and System Engineering, NC State University. harrysson@ncsu.edu

^c Professor, Orthopedic Surgery, College of Veterinary Medicine, NC State University. denis_marcellin@ncsu.edu

^d Professor, Department of Industrial and Systems Engineering, Rochester Institute of Technology. drcie@rit.edu

^e Research Professor, Dept. of Industrial and System Engineering, NC State University. hawest@ncsu.edu

^f Professor, Dept. of Industrial and System Engineering, NC State University. culbreth@ncsu.edu

Introduction

Implants serve many different functions, and thus can be made from many different materials. Orthopedic implants, which this work focuses on, mainly come from bio-inert materials such as stainless steels, cobalt-chromium alloys, titanium alloys, pure titanium and polyethylene (Zimmer 2008). The bio-inert nature of the metal orthopedic implants is derived from a highly passive surface oxide layer which quickly forms in an oxidizing environment. These materials, with the exception of polyethylene, have dramatically different mechanical properties than the surrounding bone to which they are attached (Table 3-1).

Bioresorbable metal implants are a relatively new class of implants and have been demonstrated for such things as stents (Heublein, Rohde et al. 2003). These devices are implanted into the body to serve a temporary function and are removed by resorption over

time. The resorption of metallic implants is carried out by removal of corrosion products as the metal corrodes over time. The rate of corrosion of these metal implants depends on many complex physiological factors, and is not fully understood at this time.

Recently renewed interest in magnesium alloys as bioresorbable metal implant materials has researchers excited about the prospects of load bearing reconstruction and fixation with no required subsequent surgery to remove the implant and no long term effects of leaving implants in the body. The renewed interest is primarily focused around magnesium alloys containing aluminum and/or rare earth elements (Kirkland, Lespagnol et al. 2010, Staiger, Pietak et al. 2006, Wen, Wu et al. 2009) as well as calcium based alloys (Cho, Chae et al. 2013). The primary focus around these alloys is to reduce the corrosion rate of magnesium to a rate tolerable by the body without developing subcutaneous gas bubbles. Several researchers have also done work with coatings of various magnesium alloys aimed at delaying the corrosion process until such a time when the implant is no longer necessary (Wong, Yeung et al. 2010, Ng, Wong et al. 2010, Ng, Wong et al. 2010).

Load based fixation today consists mainly of one of three primary metals - titanium, stainless steel, or cobalt chromium (Zimmer 2008). These materials are basically bio-inert, and result in little or no corrosion over the life of the implant. There has been some evidence of breakdown via abrasion and wear, and some work is ongoing to determine the effects of these wear products over time. The main disadvantage of today's implants is the relatively large gap in material properties between the bone and implant, where a phenomenon known as stress shielding occurs. The elastic modulus of these implant materials can be as much as an order of magnitude greater than that of bone. Natural bone requires stress to grow, and

areas where stress is absorbed by an implant tend to remodel, resulting in bone loss and ultimately weakening of the bone-implant interface, and loss of structural integrity. Some strategies to reduce this effect are to remove the implant after bone integrity is restored or create implant designs which reduce the effects of stress shielding by optimized implant geometry and materials (Lovald, Wagner et al. 2009).

An advantage of a bioresorbable implant is the elimination of subsequent surgeries to remove the implant. This reduces use of resources (surgeon, operating room, recovery room, etc.) and could lead to reduced health care costs and reduced complications over time. In addition, the bioresorbable implants can be doped with medicines and elements which are tuned for delivery during the healing process to reduce the incidence of infections and which promote healing of the local trauma (Di Mario, Griffiths et al. 2004).

Bioresorbable metal implants have many advantages, but several factors should be considered when designing the implants. First, any foreign material implanted in the body reacts in complex ways and is not necessarily well understood. For this reason, the quantity of foreign material should be limited to only that necessary to fulfill the role of the implant. For instance, aluminum has been linked to Alzheimers Disease (Ferreira, Piai et al. 2008, Miu, Benga 2006). Minimizing the internal exposure to aluminum should be one objective when designing implants containing aluminum for humans.

Another consideration is the bone growth around the trauma site, as in the case of children. If an implant is left too long with significant strength, bone growth may be retarded, or anomalies may be induced in the bone. However if the structural integrity of the implant-bone unit is not sufficient during the healing process, subsequent surgeries will be

necessary for stabilization. Clearly there is a window in which the failure due to corrosion of the bioresorbable implant would be optimal.

Kappatos, Chamos and Pantelakis (Kappatos, Chamos et al. 2010) developed a radial basis function neural network to estimate the effect of gradually increasing wear of AZ31 on the tensile properties. This research utilized a salt spray fog environment at 35°C for 0.5, 3, 6, 12, 24, 48 and 72 hours to which an AZ31B-O (annealed) sheet was exposed. Their short term study showed that pit depth has a stronger influence than pit density on predicting the mechanical properties.

Premature failure of magnesium alloy stents (higher than expected lumen loss) (Erbel, Di Mario et al. 2007) prompted a study for shape optimizing via finite element analysis (Wu, Petrini et al. 2010). This study performed 2D shape optimization and rolled the flat shape into a 3D tube model. Strut width increased significantly to withstand the expected loads over a longer period of time, and resulted in lower strain and stresses on critical struts. The objective of this research is to develop a model using corrosion characteristics developed from previous work to predict the expected time to failure of a magnesium AZ31 implant.

Materials and Methods

Simulated bone constructs were assembled from custom manufactured magnesium bone plates, Delrin bone segments, and magnesium cortical bone screws. The magnesium bone plates were manufactured from AZ31 magnesium alloy cold rolled to 3.2 mm thickness. These sheets were sheared and CNC machined into 114.3 by 12.7 mm plates with a set of three holes on each side of the central plane bisecting the long axis. The holes were

spaced 12.7 mm on center with 25.4 mm between the central plane and the first screw, resulting in 50.8 mm between the most central screws. The plate was filleted on all edges with a 0.8 mm radius. The plates were exposed to 100 hours of vibratory deburring and finishing with ceramic media and rinsed with ethanol prior to assembly.

The screws were custom manufactured on a Swiss-screw CNC machine using a whirling tool and rinsed with ethanol prior to assembly. The Delrin bone segments were custom machined via CNC from hollow cylinder Delrin bar stock with 25.4 mm outside diameter and 12.7 mm inside diameter. A flat surface was machined on opposite sides of the centerline to receive the bone plate. Screw holes were drilled and tapped using 3.0 mm drill bit and a 3.5 mm cortical bone screw tap. The bone plates were weighed, and the bone plates with bone screws were weighed. The simulated bone constructs were assembled and weighed as a unit. The screws were inserted by hand and torqued using a calibrated torque wrench to 0.73 N-m. A separate test determined the screw heads stripped at a torque of approximately 0.8 to 0.9 N-m, thus the relatively low final torque for these constructs. Bone plates were subjected to an immersion corrosion fatigue test based on ASTM F382-99 configuration in Hanks' Balanced Salt Solution (HBSS). Test durations were 0, 2, 4, 6, 8, 10, 14, 16, and 20 weeks. Following the immersion test, samples were cleaned with chromic acid and rinsed with ethanol. Constructs were weighed and scanned with micro-computed tomography (μ CT) at 25.4 μ m resolution. Micro CT scans were collected to observe and evaluate the pitting corrosion which AZ31 undergoes in this environment and will be used to further develop a more generic corrosion model.

Constructs were tested for mechanical properties according to ASTM F382-99. A four-point bend test was administered using a universal testing machine with major span of 127 mm and minor span of 25.4 mm. Load versus displacement data were collected on the testing machine and analyzed using a custom program written in Matlab[®]. Bending stiffness was calculated by determining the maximum slope via linear regression over 1000 points (corresponding to approximately 15.6 N). Bending strength was determined by finding the point of intercept of the load displacement data and a line parallel to and offset from the bending stiffness. The offset amount used to determine the bending strength was 1.3% of the minor span length. This offset was chosen based on the relatively slow departure from linearity that the load-displacement data exhibited.

Mathematical Modeling

Consider a simple rectangular beam that has a constant cross section across the area of interest. It is well known that the area cross section of inertia (I), without loss of generality (Oberg 2012), can be found using

$$I = \iint y^2 dA \quad 5-1$$

where y is the distance from the dA area unit to the neutral axis. Specifically for a rectangular cross section with width and height of b and h respectively, we find the area cross section of inertia for a simple rectangular beam to be

$$I = \frac{bh^3}{12} \quad 5-2$$

The deflection at the loading points of a simple beam undergoing bending where two support rollers are located on the bottom and two similar loading support rollers are located on top of the beam can be found using

$$d = W \frac{a^2(3L - 4a)}{6EI} \quad 5-3$$

where d is the displacement of the loading supports, a is the distance between loading and supporting rollers, W is the applied load of each loading roller, L is the length of the major support span, E is the material's modulus of elasticity and I is area cross section of inertia as found using Equation 5-2.

The area cross section of inertia is the only term that varies with a change of cross section. If we assume the corrosion process is random, and if the distance between loading rollers is large relative to the corrosion, then it may be possible to calculate the corrosion effect on the area cross section of inertia, even in the case of localized pitting corrosion.

An effective change in the area cross section of inertia can be found if we compare an original sample to one that has changed in some way, as in the case of corrosion over time. In our case, a set of samples were set aside as controls, and eight sets of samples were subjected to various time periods of immersion in a corrosive environment simulating *in vivo* conditions.

Noting that any difference, on average, between the flexural stiffness of corroded and non-corroded samples is due to an effective change in area cross section of inertia, one can calculate the effective corrosion rate on a simple beam by subtracting the effective area cross

section of inertia from the original value and solving for the change in cross sectional area. In this case, three surfaces of the cross section were subject to corrosive environment, while the fourth was shielded by mounting the beam (bone plate) to a simulated bone segment made of polymer. However, in general, the effective area cross section of inertia, with uniform corrosion penetration of x_1 , x_2 , x_3 , and x_4 clockwise starting with the top, can be represented by:

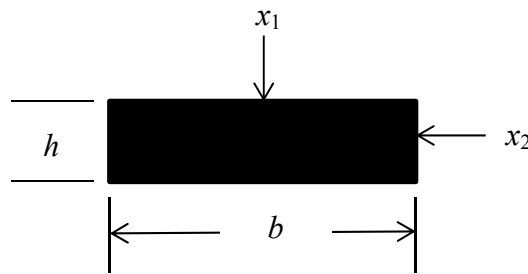


Figure 5-1 Cross section of simple beam with dimensions b and h , and corrosion penetration x_1 , x_2 , x_3 , and x_4 per side clockwise around the cross section

$$I_{eff} = \frac{(b - (x_2 + x_4))(h - (x_1 + x_3))^3}{12} \quad 5-4$$

The experiments presented here allow the following simplifying assumptions:

$$x = x_1 = x_2 = x_4 \quad 5-5$$

and

$$x_3 = 0$$

5-6

Note that x_3 is assumed to be negligible due to the fact that the surface of the implant rests directly on the bone surface and is therefore not directly exposed to the corrosive environment.

The use of Equations 5-5 and 5-6 in Equation 5-4 yields the simplified equation:

$$I_{eff} = \frac{(b - 2x)(h - x)^3}{12} \quad 5-7$$

expanding I_{eff} and reducing common terms yields:

$$I_{eff} = \frac{bh^3}{12} + \frac{(2x^4 - (6h + b)x^3 + (3hb + 6h^2)x^2 - (3bh^2 + 2h^3)x)}{12} \quad 5-8$$

Noting that the first term on the right is simply the initial area cross section of inertia prior to corrosion (Equation 5-2), then the second term on the right must represent the change of I_{eff} caused by corrosion. Therefore let

$$\Delta I = \frac{(2x^4 - (6h + b)x^3 + (3hb + 6h^2)x^2 - (3bh^2 + 2h^3)x)}{12} \quad 5-9$$

and thus

$$I_{eff} = I_0 + \Delta I \quad 5-10$$

From Equation 5-10, we can find I_{eff} from experimental data by determining the average bending stiffness for a set of samples and solving for I . Note that the average bending stiffness is simply the average of individual bending stiffness readings from multiple samples, and bending stiffness is found using linear regression applied to the load versus displacement data gathered from the 4-point bend test on the universal testing machine. Therefore

$$I_{eff} = \frac{P a^2(3L - 4a)}{d \quad 12E} \quad 5-11$$

where P/d is the average bending stiffness as discussed above, and $P = 2W$ (P is the total applied load and W is the applied load on each loading roller).

Knowing I_0 and I_{eff} , we can calculate ΔI . In the case of our example, b and h are known thus we can substitute and further simplify Equation 5-9 to obtain:

$$\Delta I = \frac{(2x^4 - 1.25x^3 + 0.28125x^2 - 0.02734375x)}{12} \quad 5-12$$

and use a non-linear solver to find x , the effective corrosion rate. A graph of ΔI per inch of corrosion for $b = 12.7$ mm and $h = 3.2$ mm is presented in Figure 5-2.

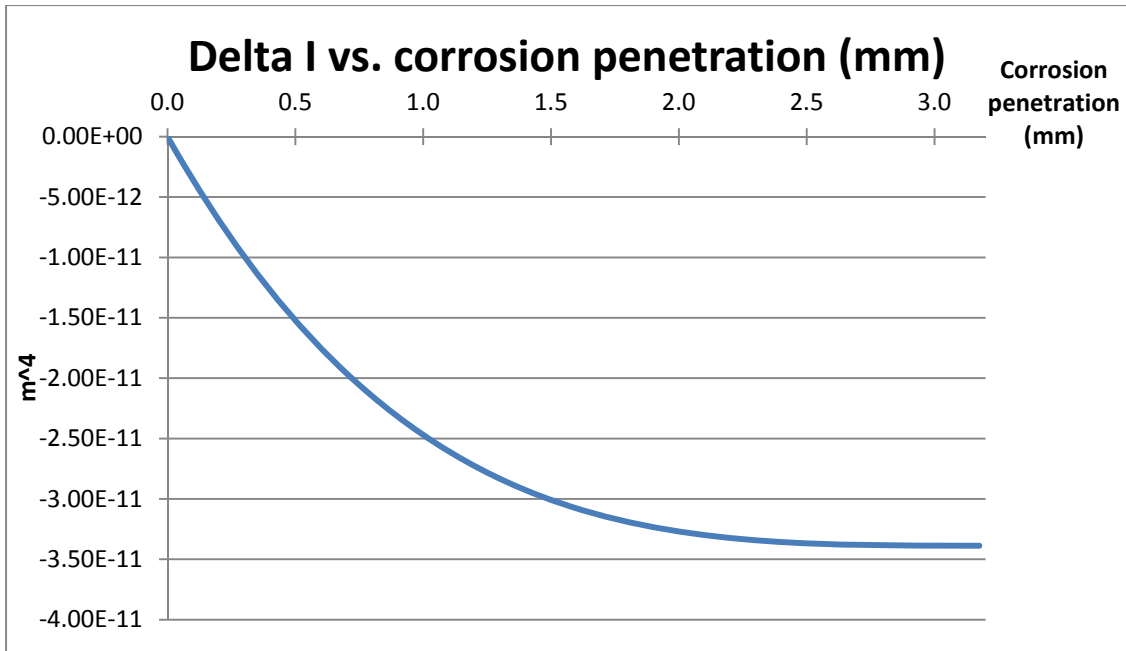


Figure 5-2 Graph of ΔI per mm of corrosion

The yield stress at the most distant point from the central or neutral axis (the point which experiences the greatest tensile stress and strain) is calculated using:

$$\sigma = \frac{My}{I} \quad 5-13$$

where the yield stress of AZ31B-H24 is 213 MPa, and y is the distance from the farthest fiber to the neutral axis. The moment (M) of the example constructs tested is calculated as follows:

$$M = \frac{PL}{2} - \frac{Pa}{2} \quad 5-14$$

where $L = 127$ mm and $a = 25.4$ mm and P is applied load. Therefore the moment reduces to

$$M = 0.0254P \quad 5-15$$

Both I and y following immersion in a corrosive media are functions of the corrosion penetration; I as described in Equation 5-4 and

$$y = \frac{h - x}{2} \quad 5-16$$

Finally using Equations 5-8, 5-13, 5-15, and 5-16 we arrive at

$$\frac{P}{\sigma} = \frac{I_0 + \Delta I(f(x))}{y(f(x))} \quad 5-17$$

We define the failure point of an implant as the point where yield stress is exceeded. This point is dependent on geometry as detailed above, and x is a function of time in a corrosive environment. We can estimate the useful life of an implant by pre-determining an expected maximum load the implant will be subjected to and then calculating the ΔI and y where the stress is exceeded. Finally, determining the expected life of the implant is a matter of determining the length of time that it takes for the corresponding corrosion penetration to occur, either via a lookup table or via estimated corrosion rate.

In our case, normalization of I and y was required to account for departures of the construct from normal assumptions, i.e. constant cross section across the entire length of the

specimen, and simple supporting structures located on the beam itself. In the case of I , the cross sectional area of inertia for the specific beam geometry was calculated and compared to that found via Equation 5-11 for samples that had not been exposed to corrosion media. This was normalized using a simple ratio multiplier. In a similar fashion, the expected y (distance from neutral axis to the most distant tensile fiber) was determined by solving Equation 5-16 given $x = 0$.

Results

Estimates for corrosion penetration were calculated using Equation 5-12 for cyclic, non-loaded and statically loaded samples (Table 5-1, Table 5-2, Table 5-3). Bending strength estimates were calculated using corrosion estimates and Equation 5-17. A graph of the estimated corrosion as determined using Equation 5-12 is presented in Figure 5-3.

Table 5-1 Bending Strength (N-m) comparison and corrosion depth (mm) estimate for cyclic loaded samples

Week	Cyclic Loaded			Corrosion Estimate (mm)
	Actual (N-m)	Estimate (N-m)	Error (%)	
2	4.14	4.67	12.9%	0.16
4	3.73	4.36	17.1%	0.26
6	3.20	4.06	26.9%	0.37
8	2.70	3.76	39.1%	0.49
10	3.11	4.09	31.8%	0.36
14	2.67	3.78	41.8%	0.48
16	2.38	3.46	45.5%	0.61
20	0	0	N/A	

Table 5-2 Bending Strength (N-m) comparison and corrosion depth (mm) estimate for non-loaded samples

Week	Non-Loaded			Corrosion Estimate (mm)
	Actual (N-m)	Estimate (N-m)	Error (%)	
2	4.53	4.93	9.0%	0.07
4	4.25	4.71	11.0%	0.14
6	3.93	4.47	13.8%	0.22
8	3.71	4.28	15.3%	0.29
10	4.10	4.58	11.7%	0.19
14	3.67	4.34	18.1%	0.27
16	3.13	3.92	25.3%	0.42
20	2.51	3.55	41.5%	0.57

Table 5-3 Bending Strength (N-m) comparison and corrosion depth (mm) estimate for statically loaded samples

Week	Static Loaded			Corrosion Estimate (mm)
	Actual (N-m)	Estimate (N-m)	Error (%)	
2	4.41	4.83	9.6%	0.11
4	3.98	4.56	14.7%	0.19
6	3.68	4.35	18.3%	0.26
8	3.60	4.28	18.9%	0.29
10	3.37	4.17	24.0%	0.33
14	3.03	3.94	29.9%	0.42
16	2.49	3.64	46.3%	0.54
20	1.74	2.98	71.9%	0.85

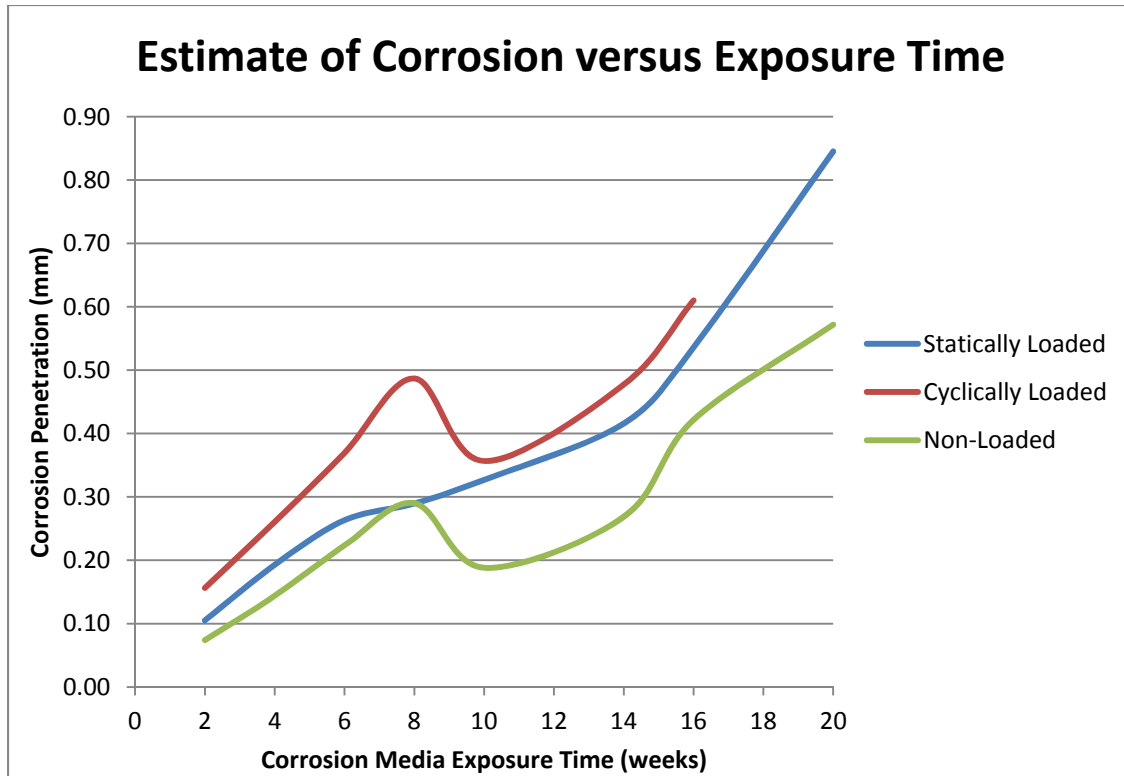


Figure 5-3 Estimate of the surface corrosion depth for different loading conditions per exposure time

Discussion

Bending strength estimates using the described method result in errors between 9-72% (Table 5-1, Table 5-2, and Table 5-3). Not surprisingly, the error climbs substantially as samples remain in the corrosive environment for longer periods of time. Estimates for non-loaded constructs appear to be closer to actual measured bending strengths than for cyclically or statically loaded samples. This result follows intuition, since crack development caused by static (stress corrosion cracking) or cyclic (fatigue) loading would concentrate stress and

cause the actual yield load to be lower than expected (i.e. the model does not account for crack formation).

A modified construct was fitted with strain gages on the top and bottom magnesium surfaces to measure the compressive strain and tensile strain through the elastic region. Normal 4-point bend test results were verified when strain indications agreed within 2% with the assumed neutral axis being located in the center of the cross section.

The assumption of neutral axis shift ($y = (h - x)/2$) was revisited by physical comparison and measurement (Figure 5-4). The left most screw is shown nearly completely intact, and the plate in this region shows virtually no corrosion. Visual comparison across the length of the plate shows little degradation even in the area of maximum stress between the loading rollers. This implies that calculation of the bending moment necessary to impart permanent deformation using a departure of the neutral plane based on Equation 5-16 may not be appropriate.

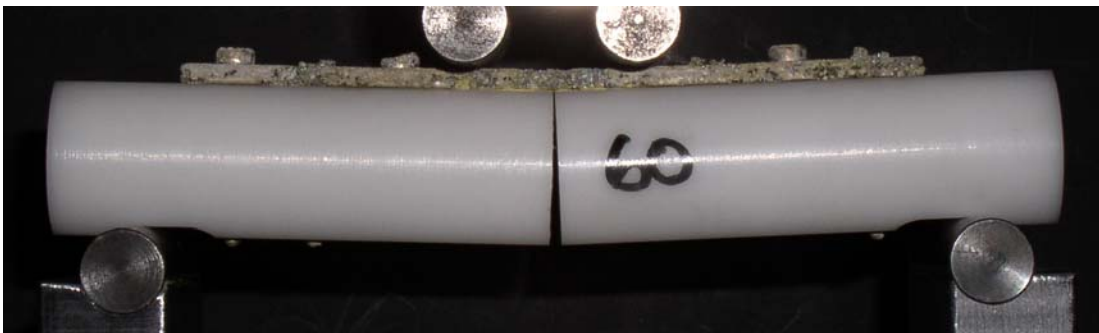


Figure 5-4 Construct with lowest measured bending stiffness (14,571 N/m) and highest implied corrosion. Visual inspection shows much less corrosion penetration than predicted (predicted > 0.84 mm, original plate thickness = 3.2 mm)

Bending strength estimates using $y = 1.6$ mm, half of the original thickness of 3.2 mm result in a closer approximation of the actual bending strength (Table 5-4, Table 5-5 and Table 5-6)

The corrosion estimates predict general corrosion (i.e., the reduction of strength is uniform across the region of interest), however the corrosion mode is known to be pitting corrosion (Atrens, Liu et al. 2011) and is clearly observed as such in Figure 5-5 and Figure 5-7, further justifying a departure from the neutral axis shift assumption.

Table 5-4 Bending Strength (N-m) comparison and corrosion depth (mm) estimate for cyclically loaded samples with $y = 1.6$ mm (assumed constant throughout test)

Week	Cyclic Loaded			Corrosion Estimate (mm)
	Actual (N-m)	Estimate (N-m)	Error	
2	4.14	4.44	7.3%	0.16
4	3.73	4.00	7.5%	0.26
6	3.20	3.59	12.2%	0.37
8	2.70	3.18	17.7%	0.49
10	3.11	3.63	17.0%	0.36
14	2.67	3.21	20.4%	0.48
16	2.38	2.80	17.5%	0.61
20	0.00	0	N/A	0

Table 5-5 Bending Strength (N-m) comparison and corrosion depth (mm) estimate for non-loaded samples with $y = 1.6$ mm (assumed constant throughout test)

Week	Non-Loaded			Corrosion Estimate (mm)
	Actual (N-m)	Estimate (N-m)	Error	
2	4.53	4.82	6.5%	0.07
4	4.25	4.50	5.9%	0.14
6	3.93	4.16	5.8%	0.22
8	3.71	3.89	4.8%	0.29
10	4.10	4.30	5.1%	0.19
14	3.67	3.97	8.1%	0.27
16	3.13	3.40	8.6%	0.42
20	2.51	2.91	16.0%	0.57

Table 5-6 Bending Strength (N-m) comparison and corrosion depth (mm) estimate for statically loaded samples with $y = 1.6$ mm (assumed constant throughout test)

Week	Static Loaded			Corrosion Estimate (mm)
	Actual (N-m)	Estimate (N-m)	Error	
2	4.41	4.67	6.0%	0.11
4	3.98	4.29	7.7%	0.19
6	3.68	3.99	8.5%	0.26
8	3.60	3.89	8.1%	0.29
10	3.37	3.74	11.2%	0.33
14	3.03	3.42	12.9%	0.42
16	2.49	3.02	21.6%	0.54
20	1.74	2.19	26.1%	0.85

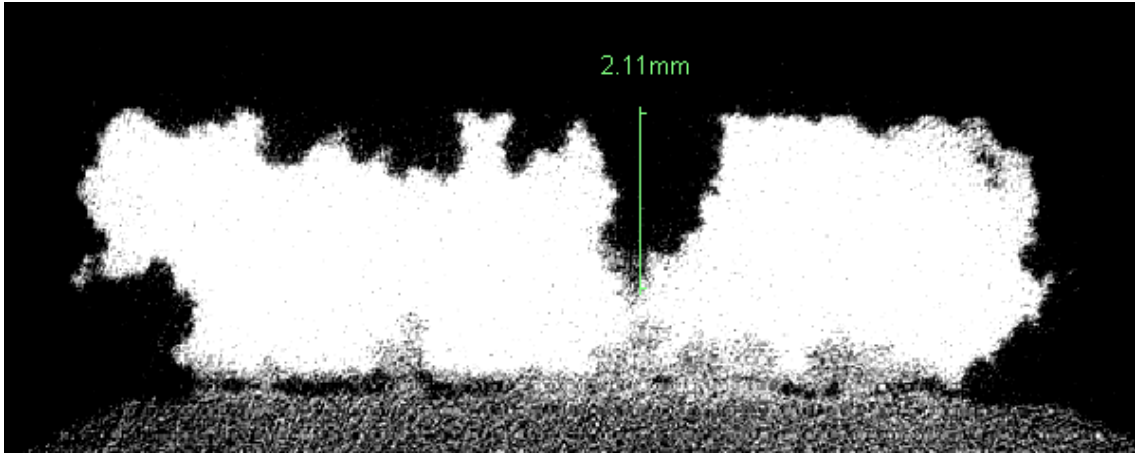


Figure 5-5 Micro CT image of construct 58 (cyclic loading) after 12 weeks exposure to corroding medium. Measured pit depth is 2.11 mm, original thickness = 3.2 mm

The pitting manifestation in Figure 5-5 shows a 2.11 mm depth pit from a cyclically loaded construct. Overall thickness of the original bone plate was 3.2 mm, resulting in a penetration of 66%. Figure 5-5 shows the largest pit depth from sample construct 58 which was subjected to 80 days of cyclic loading and 12 weeks of immersion in Hanks solution. The μ CT image was taken on the longitudinal axis (Figure 5-6) of the bone construct at a resolution of 25.4 μ m per pixel. The μ CT image was limited to the region between screw sets due to the machine capacity.

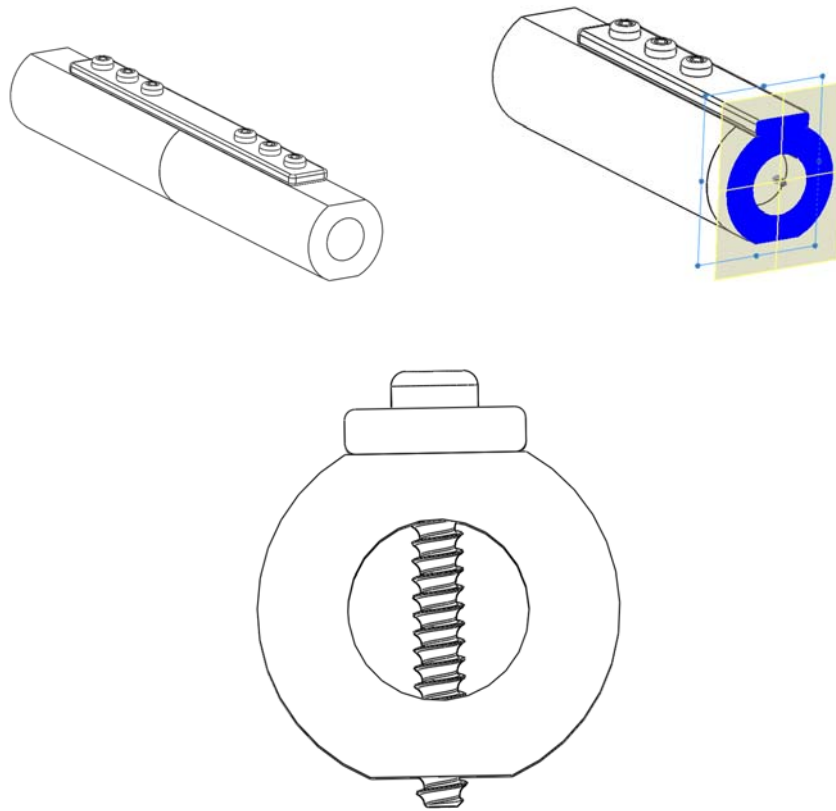


Figure 5-6 View of construct from various positions. Top left is a model of the bone construct, top right is the approximate section plane of the radiographic slice in Figure 5-5, bottom is the view normal to section plane

The pitting corrosion density and penetration can also be observed in Figure 5-7. A non-corroded sample was scanned via μ CT for reference. A scan of construct number 92, which was exposed to 10 weeks of cyclic loading while immersed, along with the reference scan, was converted to a triangulated surface model via Mimics Innovation Suite from Materialise NV (Plymouth, Michigan). The two scans were manually aligned within 3-Matic software from Materialise NV, and a Boolean subtraction was performed. The resulting triangulated surface model representing the size and distribution of pits shows relatively few pits and modest corrosion penetration. The top image shown in isometric view covers

roughly the entire scan area (approximately 50.8 mm). The lower left image is taken from the longitudinal axis (Figure 5-6), and the lower right image is from the underside of the simulated bone plate (approximately 50.8 mm in length and 12.7 mm in width).

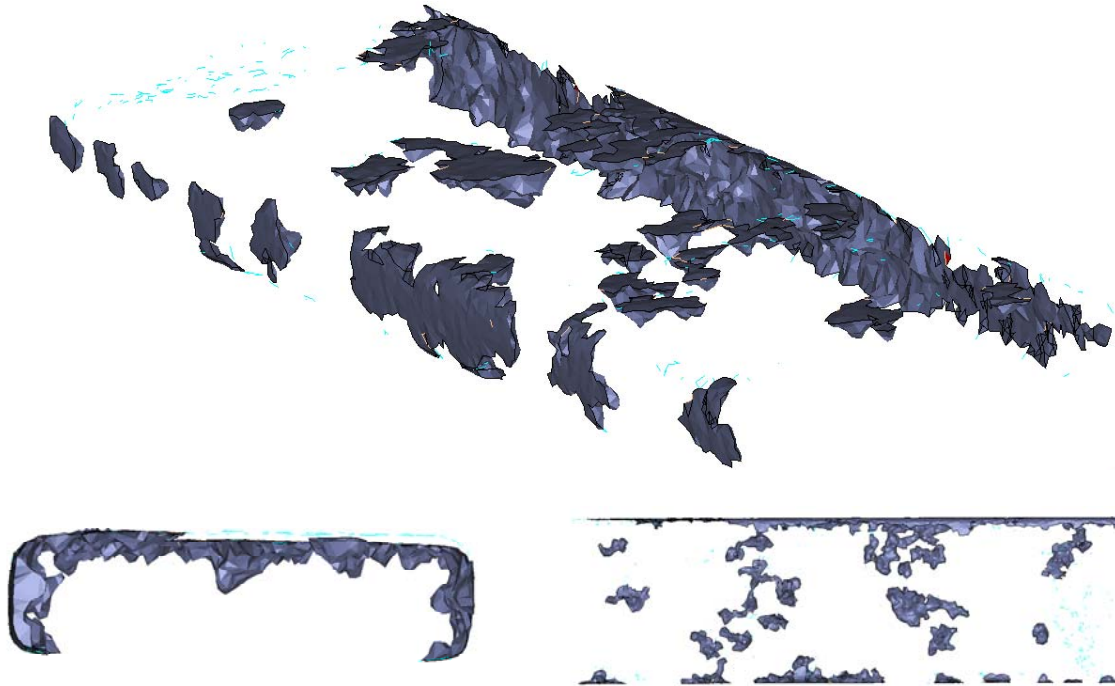


Figure 5-7 Triangulated surface model of a boolean subtraction of a non-corroded sample and a corroded sample. Data reconstructed from μ CT data

The simplifying assumptions made here clearly affect the long range accuracy of the model in predicting the time to failure of an implant *in vitro*. It was found during this study that a much closer approximation of the failure load could be found by changing Equation 5-16 to:

$$y = \frac{h + x}{2} \quad 5-18$$

however, no mathematical justification could be found for doing so, and thus is considered for future work.

It is clear that while this model provides a reasonable starting point, more work needs to be done. The current model is based on specific geometry and assumptions that over time lead to significant inaccuracies. However, considering the consolidation time for long bone fractures in children is 5-25 weeks (Berger, De Graaf et al. 2005) with a mean of 12 weeks using a flexible fixation method, the errors of current model (approximately 20%) are reasonable considering the randomness of the corrosion process.

A second data set, from work done in Chapter 3, was tested using this method. Equation 5-7 was modified to include corrosion on all 4 sides of the cross section:

$$I_{eff} = \frac{(b - 2x)(h - 2x)^3}{12} \quad 5-19$$

This is reasonable considering the underside corrosion seen in Figure 5-7. Although the underside of the implant is not exposed to the moving fluid, the lack of water tight seal between the implant and the bone surfaces suggest that corrosion will still occur there. Results presented in Table 5-7 show agreement within 16.5%, validating the model for situations where corroding medium caused corrosion on 4 sides of the cross section.

Table 5-7 Bending strength estimates of data acquired in Chapter 3 (N-m)

Week	Actual (N-m)	Estimate (N-m)	Error (N-m)	Error (%)
0	2.37	2.76	0.39	16.5%
2	2.61	2.46	-0.15	-5.6%
4	2.80	2.44	-0.35	-12.6%
6	2.51	2.60	0.09	3.5%
8	2.62	2.66	0.05	1.7%
10	2.24	2.51	0.27	12.0%
12	2.32	2.58	0.26	11.4%
14	2.26	2.50	0.23	10.4%
16	2.08	2.35	0.27	12.9%
18	2.16	2.37	0.21	9.6%
20	2.19	2.42	0.23	10.7%

Future work

While the current model provides a first order approximation for predicting resorbable metal implant failure, future work will include modeling pitting corrosion on a generalized surface to allow for optimized and custom bone fixation. Simple beam assumptions will not work on those instances, therefore physics based modeling (finite element analysis) will be employed. The resulting model will be validated using data collected for this experiment.

Investigation of the cyclic and static loading effects needs to be further evaluated and incorporated into the model. The trend of the errors tends to increase with time, which may be expected as the simple cross sectional beam assumption becomes less appropriate as the pit size increases relative to the fixed distance between loading rollers. Modeling the pitting

corrosion phenomenon is considered essential to creating an accurate model of the strength degradation.

Conclusion

A mathematical model predicting the time to failure of magnesium alloy AZ31 was presented. The model predicts the time to failure to $\pm 26\%$ of the experimentally observed time to failure. The model uses a generalized estimate of corrosion penetration to predict the change in the area of inertia, and ultimately the bending strength, and can be used to predict time to failure of biodegradable metallic implants of any alloy provided corrosion rate estimates are available.

6. FUTURE WORK AND CONCLUSION

Future Work

Consideration of magnesium and magnesium alloys for use in bioresorbable devices has grown rapidly in recent years as evidenced by the large number of research articles published in the past 15 years. Primary consideration has been given to the rapid rate at which various magnesium alloys corrode in environments similar to those encountered *in vivo*. Magnesium's high placement on the galvanic activity chart along with the susceptibility to pitting corrosion in the presence of chlorides results in many alloys which are not suitable for implantation into a physiological environment. Rapid corrosion causes subcutaneous gas bubble formation and could lead to unfavorable physiological responses as well as premature failure of load bearing implants.

The rapid corrosion rate has led researchers to focus on developing new alloys, including those with rare earth elements, various amounts of aluminum and zinc, and calcium. The efforts focus on achieving an appropriate corrosion rate where the hydrogen evolution from the corrosion process matches what the physiological system can process. Other research has focused on developing coatings, including cerium, stearic acid, and anodizing which prevent the onset of attack of the base metal during the healing process. However, if the coating is compromised during surgical installation or during the manufacturing process, the system may fail prematurely.

Alloying elements such as aluminum have been linked to Alzheimer susceptibility. Rare earth elements have not been studied for long term cellular response in many of the possible implant alloys. The exposure to these elements should therefore be minimized until their safety is established. The research presented in Chapter 5 presents a first order approximation the failure point of an implant based on corrosion rates and some simple geometry approximations. However, much work needs to be done.

Minimizing elemental exposure requires custom solutions for each patient, for every fracture and fixation requirement is different. Different load carrying requirements, different geometric requirements, and different healing rates of patients are just some examples of the complexities of creating a custom fixation system which minimizes the exposure of patients to foreign elements.

The extension of the work presented in Chapters 2-5 is intended to take some of these issues into consideration. A general discussion of intended and needed work follows.

In vivo testing

In vivo work to this point has involved small scale studies to measure animal response to various alloys. Measurements of *in vivo* corrosion rate, while attempted, have not resulted in any general agreement among researchers. To complicate matters, corrosion rates differ species to species, as well as by location within the body. It has been shown that exposure to soft tissue, to cortical bone and to trabecular bone all result in different corrosion rates. More work to determine *in vivo* corrosion rates at these locations and others is necessary to predict the service life of an implant.

Many different alloys and coatings have been developed and applied to magnesium implant research. A number of these have been tested *in vivo*, but many have not. The expense of *in vivo* studies points to a need to develop *in vitro* testing models which more closely approximate *in vivo* conditions. This requires further understanding of the physiological response to the foreign material: localized pH conditions, fluid flow conditions, localized chloride and other element levels, corrosion product migration, bone response to alloying elements, and other conditions are not well understood and need to be studied to improve *in vitro* testing. More work needs to be done in this area to help researchers analyze prospective alloys prior to expensive *in vivo* testing.

Modeling

The simple failure model estimate presented in Chapter 5 needs to be extended. Minimizing the amount of material implanted would reduce exposure to various alloying elements and would reduce exposure to foreign bodies, which the body fights with various physiological responses. This requires custom implants with topology optimization which will not conform well to simple beam geometry and analysis. Additionally, consideration for failure of the system (fixation plate, screws and biological tissue) should be built into any model used by a surgeon.

The ideal system would include the capability to read x-ray and/or CT data, evaluate expected loads based on patient parameters such as age, weight, activity level, and growth expectations, optimize a shape and alloy, and present a custom implant model specific for the patient and fracture location. This model could then be manufactured *in situ* and installed in

the patient. Estimating the corrosion response for a generalized surface is the next step in this research.

Conclusion

Magnesium alloy AZ31 was evaluated for potential use as a bioresorbable fixation material. Results from our initial study show potential for solid magnesium plates to maintain load carrying capabilities longer than porous or traditional style plates with holes evenly spaced throughout the length.

Further testing was performed to evaluate the performance of AZ31 in static load and corrosion fatigue environments. Constructs exposed to corrosion fatigue showed significantly lower bending strengths than either non-loaded or statically-loaded constructs. Constructs exposed to static loads had reduced bending strengths as compared to non-loaded samples for time periods longer than 10 weeks. When considering AZ31 for a load bearing implant, the expected loading should be taken into consideration as the load carrying life span is impacted by these loads. The AZ31 alloy may be appropriate for fixation in situations where the healing time is short, such as the case in young animals, or where activity level is lower, such as in older animals. With mechanical properties closer to those observed in actual bone, magnesium alloys could reduce the stress shielding effect seen in traditional implants. If coated with a corrosion inhibitor, they could increase the time to failure of the implant. It is noted that highly active and relatively slower healing patients may not be appropriate candidates for using AZ31 as implant materials for fixation.

A mathematical model was found to estimate the useful life of a load bearing bioresorbable implant based on beam analysis. The model is able to predict the bending strength based on estimates of the corrosion rate applied to one or more surfaces of a simple beam. The model was applied to two different data sets and estimates of the bending strength agreed within 30% of experimental results.

REFERENCES

- ASTM Standard F382, 1999 (2008), "Standard Specification and Test Method for Metallic Bone Plates," ASTM International, West Conshohocken, PA, 2008, DOI: 10.1520/F0382-99R08E01, www.astm.org.
- AMBAT, R., AUNG, N.N. and ZHOU, W., 2000. Evaluation of microstructural effects on corrosion behaviour of AZ91D magnesium alloy. *Corrosion Science*, **42**(8), pp. 1433-1455.
- ARAUJO, M.M., WAITE, P.D. and LEMONS, J.E., 2001. Strength analysis of Le Fort I osteotomy fixation: titanium versus resorbable plates. *Journal of oral and maxillofacial surgery*, **59**(9), pp. 1034-1039.
- ATRENS, A., LIU, M. and ZAINAL ABIDIN, N.I., 2011. Corrosion mechanism applicable to biodegradable magnesium implants. *Materials Science and Engineering: B*, **176**(20), pp. 1609-1636.
- AVEDSIAN, M.M. and BAKER, H., eds, 1999. *Magnesium and Magnesium Alloys*. Materials Park, OH: ASM International.
- BERGER, P., DE GRAAF, J.S. and LEEMANS, R., 2005. The use of elastic intramedullary nailing in the stabilisation of paediatric fractures. *Injury*, **36**(10), pp. 1217-1220.
- CHO, S.Y., CHAE, S., CHOI, K.W., SEOK, H.K., KIM, Y.C., JUNG, J.Y., YANG, S.J., KWON, G.J., KIM, J.T. and ASSAD, M., 2013. Biocompatibility and strength retention of biodegradable Mg-Ca-Zn alloy bone implants. *Journal of Biomedical Materials Research Part B: Applied Biomaterials*, **101B**(2), pp. 201-212.
- DI MARIO, C., GRIFFITHS, H., GOKTEKIN, O., PEETERS, N., VERBIST, J., BOSIERS, M., DELOOSE, K., HEUBLIN, B., ROHDE, R., KASSE, V., ILSLEY, C. and ERBEL, R., 2004. Drug-Eluting Bioabsorbable Magnesium Stent. *Journal of interventional cardiology*, **17**(6), pp. 391-395.
- ERBEL, R., DI MARIO, C., BARTUNEK, J., BONNIER, J., DE BRUYNE, B., EBERLI, F.R., ERNE, P., HAUDE, M., HEUBLEIN, B. and HERRIGAN, M., 2007. Temporary scaffolding of coronary arteries with bioabsorbable magnesium stents: a prospective, non-randomised multicentre trial. *The Lancet*, **369**(9576), pp. 1869-1875.
- FEKRY, A.M. and EL-SHERIF, R.M., 2009. Electrochemical corrosion behavior of magnesium and titanium alloys in simulated body fluid. *Electrochimica Acta*, **54**(28), pp. 7280-7285.

- FERREIRA, P., PIAI, K., TAKAYANAGUI, A. and SEGURA-MUNOZ, S., 2008. Aluminum as a Risk Factor for Alzheimer's Disease. *Rev Lat Am Enfermagem*, **16**(1), pp. 151.
- FONTANA, M.G. and GREEN, N., D., 1978. *Corrosion Engineering*. New York: McGraw Hill.
- GU, X.N., ZHOU, W.R., ZHENG, Y.F., LIU, Y. and LI, Y.X., 2010. Degradation and cytotoxicity of lotus-type porous pure magnesium as potential tissue engineering scaffold material. *Materials Letters*, **64**(17), pp. 1871-1874.
- GU, X., ZHENG, Y., CHENG, Y., ZHONG, S. and XI, T., 2009. *In vitro* corrosion and biocompatibility of binary magnesium alloys. *Biomaterials*, **30**(4), pp. 484-498.
- HEUBLEIN, B., ROHDE, R., KAESE, V., NIEMEYER, M., HARTUNG, W. and HAVERICH, A., 2003. Biocorrosion of magnesium alloys: a new principle in cardiovascular implant technology? *Heart*, **89**(6), pp. 651-656.
- HU, J., WANG, C., REN, W.C., ZHANG, S. and LIU, F., 2010. Microstructure evolution and corrosion mechanism of dicalcium phosphate dihydrate coating on magnesium alloy in simulated body fluid. *Materials Chemistry and Physics*, **119**(1-2), pp. 294-298.
- HUSE, E.C., 1878. A New Ligature. *Chicago Medical Journal and Examiner*, **37**, pp. 171-172.
- JACOBS, J.J., GILBERT, J.L. and URBAN, R.M., 1998. Current Concepts Review - Corrosion of Metal Orthopaedic Implants. *Journal of Bone and Joint Surgery*, **80**(2), pp. 268-82.
- KANG, Y., YAO, Y., YIN, G., HUANG, Z., LIAO, X., XU, X. and ZHAO, G., 2009. A study on the *in vitro* degradation properties of poly(l-lactic acid)/ β -tricalcium phosphate(PLLA/ β -TCP) scaffold under dynamic loading. *Medical engineering & physics*, **31**(5), pp. 589-594.
- KANNAN, M.B., 2010. Influence of microstructure on the *in vitro* degradation behaviour of magnesium alloys. *Materials Letters*, **64**(6), pp. 739-742.
- KANNAN, M.B. and RAMAN, R.K.S., 2008. *In vitro* degradation and mechanical integrity of calcium-containing magnesium alloys in modified-simulated body fluid. *Biomaterials*, **29**(15), pp. 2306-2314.

- KAPPATOS, V., CHAMOS, A.N. and PANTELAKIS, S.G., 2010. Assessment of the effect of existing corrosion on the tensile behaviour of magnesium alloy AZ31 using neural networks. *Materials & Design*, **31**(1), pp. 336-342.
- KIM, Y., KIM, Y., YUN, P. and KIM, J., 2009. Evaluation of skeletal and surgical factors related to relapse of mandibular setback surgery using the bioabsorbable plate. *Journal of Cranio-Maxillofacial Surgery*, **37**(2), pp. 63-68.
- KIRKLAND, N.T., LESPAGNOL, J., BIRBILIS, N. and STAIGER, M.P., 2010. A survey of bio-corrosion rates of magnesium alloys. *Corrosion Science*, **52**(2), pp. 287-291.
- KNOTHE TATE, M.L., 2003. "Whither flows the fluid in bone?" An osteocyte's perspective. *Journal of Biomechanics*, **36**(10), pp. 1409-1424.
- LEE, H., OH, J., KIM, S., KIM, H., MOON, S., KIM, Y., YUN, P. and SON, J., 2010. Comparison of titanium and biodegradable miniplates for fixation of mandibular fractures. *Journal of Oral and Maxillofacial Surgery*, **68**(9), pp. 2065-2069.
- LHOTKA, C., SZEKERES, T., STEFFAN, I., ZHUBER, K. and ZWEYMÜLLER, K., 2003. Four-year study of cobalt and chromium blood levels in patients managed with two different metal-on-metal total hip replacements. *Journal of Orthopaedic Research*, **21**(2), pp. 189-195.
- LOVALD, S.T., WAGNER, J.D. and BAACK, B., 2009. Biomechanical Optimization of Bone Plates Used in Rigid Fixation of Mandibular Fractures. *Journal of Oral and Maxillofacial Surgery*, **67**(5), pp. 973-985.
- MCBRIDE, E.D., 1938. Magnesium Screw and Nail Transfixion in Fractures. *Southern medical journal*, **31**(5), pp. 508-514.
- MIDDLETON, J.C. and TIPTON, A.J., 2000. Synthetic biodegradable polymers as orthopedic devices. *Biomaterials*, **21**(23), pp. 2335-2346.
- MIU, A.C. and BENGA, O., 2006. Aluminum and Alzheimer's disease: A new look. *Journal of Alzheimer's Disease*, **10**(2), pp. 179-201.
- NAN, Z.Y., ISHIHARA, S. and GOSHIMA, T., 2008. Corrosion fatigue behavior of extruded magnesium alloy AZ31 in sodium chloride solution. *International Journal of Fatigue*, **30**(7), pp. 1181-1188.
- NATIONAL INSTITUTES OF HEALTH, 7/13/2009, 2009-last update, NIH Magnesium Factsheet. Available: <http://ods.od.nih.gov/factsheets/magnesium.asp> [7/12, 2010].

NG, W.F., WONG, M.H. and CHENG, F.T., 2010. Cerium-based coating for enhancing the corrosion resistance of bio-degradable Mg implants. *Materials Chemistry and Physics*, **119**(3), pp. 384-388.

NG, W.F., WONG, M.H. and CHENG, F.T., 2010. Stearic acid coating on magnesium for enhancing corrosion resistance in Hanks' solution. *Surface and Coatings Technology*, **204**(11), pp. 1823-1830.

OBERG, E., 2012. *Machinery's Handbook 29th Edition Large Print electronic resource*. New York: Industrial Press.

PIETRZAK, W.S. and EPPLEY, B.L., 2000. Resorbable polymer fixation for craniomaxillofacial surgery: development and engineering paradigms. *The Journal of craniofacial surgery*, **11**(6), pp. 575.

PIIPER, J., CANFIELD, R. and RAHN, H., 1962. Absorption of various inert gases from subcutaneous gas pockets in rats. *Journal of applied physiology*, **17**(2), pp. 268-274.

PULEO, D.A. and HUH, W.W., 1995. Acute toxicity of metal ions in cultures of osteogenic cells derived from bone marrow stromal cells. *Journal of Applied Biomaterials*, **6**(2), pp. 109-116.

RETTIG, R. and VIRTANEN, S., 2008. Time-dependent electrochemical characterization of the corrosion of a magnesium rare-earth alloy in simulated body fluids. *Journal of Biomedical Materials Research Part A*, **85A**(1), pp. 167-175.

ROMANI, A. and SCARPA, A., 2000. Regulation of cellular magnesium. *Front Biosci*, **5**, pp. D720-D734.

RUBIN, H., 2005. Degrees and kinds of selection in spontaneous neoplastic transformation: An operational analysis. *Proceedings of the National Academy of Sciences of the United States of America*, **102**(26), pp. 9276-9281.

RUBIN, H., 2005. Magnesium: the missing element in molecular views of cell proliferation control. *Bioessays*, **27**(3), pp. 311-320.

SALUNKE, P., SHANOV, V. and WITTE, F., 2011. High purity biodegradable magnesium coating for implant application. *Materials Science and Engineering: B*, **176**(20), pp. 1711-1717.

SCIENCEDIRECT.COM, 2010-last update, Online Search of journal articles. Available: http://www.sciencedirect.com/science?_ob=ArticleListURL&_method=list&_ArticleListID=

[1214619301&_sort=d&view=c&_acct=C000015398&_version=1&_urlVersion=0&_userid=6683130&md5=3094100cc86563c94a2671dca5ff6578](https://doi.org/10.1002/1522-2675(201002)49:4%3E1696::AID-CORR1696%3E3.0.CO;2-1) [2/20/2010, 2010].

SONG, G. and ATRENS, A., 2004. Understanding magnesium corrosion—A framework for improved alloy performance. *Advanced engineering materials*, **5**(12), pp. 837-858.

SONG, G., 2007. Control of biodegradation of biocompatible magnesium alloys. *Corrosion Science*, **49**(4), pp. 1696-1701.

STAIGER, M.P., PIETAK, A.M., HUADMAI, J. and DIAS, G., 2006. Magnesium and its alloys as orthopedic biomaterials: A review. *Biomaterials*, **27**(9), pp. 1728-1734.

SUURONEN, R., POHJONEN, T., HIETANEN, J. and LINDQVIST, C., 1998. A 5-year *in vitro* and *in vivo* study of the biodegradation of polylactide plates. *Journal of oral and maxillofacial surgery*, **56**(5), pp. 604-614.

TAHAN, J.E., GRANADILLO, V.A. and ROMERO, R.A., 1994. Electrothermal atomic absorption spectrometric determination of Al, Cu, Fe, Pb, V and Zn in clinical samples and in certified environmental reference materials. *Analytica Chimica Acta*, **295**(1-2), pp. 187-197.

WAKSMAN, R., ERBEL, R., DI MARIO, C., BARTUNEK, J., DE BRUYNE, B., EBERLI, F.R., ERNE, P., HAUDE, M., HERRIGAN, M. and ILSLEY, C., 2009. Early-and long-term intravascular ultrasound and angiographic findings after bioabsorbable magnesium stent implantation in human coronary arteries. *JACC: Cardiovascular Interventions*, **2**(4), pp. 312-320.

WAKSMAN, R., PAKALA, R., BAFFOUR, R., SEABRON, R., HELLINGA, D. and TIO, F.O., 2008. Short-Term Effects of Biocorrosible Iron Stents in Porcine Coronary Arteries. *Journal of interventional cardiology*, **21**(1), pp. 15-20.

WAKSMAN, R., PAKALA, R., KUCHULAKANTI, P.K., BAFFOUR, R., HELLINGA, D., SEABRON, R., TIO, F.O., WITTCHOW, E., HARTWIG, S. and HARDER, C., 2006. Safety and efficacy of bioabsorbable magnesium alloy stents in porcine coronary arteries. *Catheterization and cardiovascular interventions*, **68**(4), pp. 607-617.

WAKSMAN, R., PAKALA, R., OKABE, T., HELLINGA, D., CHAN, R., TIO, M.O., WITTCHOW, E., HARTWIG, S., WALDMANN, K. and HARDER, C., 2007. Efficacy and safety of absorbable metallic stents with adjunct intracoronary beta radiation in porcine coronary arteries. *Journal of interventional cardiology*, **20**(5), pp. 367-372.

WANG, H., ESTRIN, Y. and ZÚBEROVÁ, Z., 2008. Bio-corrosion of a magnesium alloy with different processing histories. *Materials Letters*, **62**(16), pp. 2476-2479.

- WANG, L., SHINOHARA, T., ZHANG, B. and IWAI, H., 2009. Characterization of surface products on AZ31 magnesium alloy in dilute NaCl solution. *Journal of Alloys and Compounds*, **485**(1-2), pp. 747-752.
- WANG, Y.M., WANG, F.H., XU, M.J., ZHAO, B., GUO, L.X. and OUYANG, J.H., 2009. Microstructure and corrosion behavior of coated AZ91 alloy by microarc oxidation for biomedical application. *Applied Surface Science*, **255**(22), pp. 9124-9131.
- WEN, Z., WU, C., DAI, C. and YANG, F., 2009. Corrosion behaviors of Mg and its alloys with different Al contents in a modified simulated body fluid. *Journal of Alloys and Compounds*, **488**(1), pp. 392-399.
- WITTE, F., ELIEZER, A. and COHEN, S., 2010. The History, Challenges and the Future of Biodegradable Metal Implants. *Advanced Materials Research*, **95**, pp. 3-7.
- WITTE, F., KAESE, V., HAFERKAMP, H., SWITZER, E., MEYER-LINDENBERG, A., WIRTH, C.J. and WINDHAGEN, H., 2005. *In vivo* corrosion of four magnesium alloys and the associated bone response. *Biomaterials*, **26**(17), pp. 3557-3563.
- WITTE, F., ULRICH, H., PALM, C. and WILLBOLD, E., 2007. Biodegradable magnesium scaffolds: Part II: Peri-implant bone remodeling. *Journal of Biomedical Materials Research Part A*, **81**(3), pp. 757-765.
- WITTE, F., ULRICH, H., RUDERT, M. and WILLBOLD, E., 2007. Biodegradable magnesium scaffolds: Part 1: appropriate inflammatory response. *Journal of Biomedical Materials Research Part A*, **81**(3), pp. 748-756.
- WITTE, F., FISCHER, J., NELLESEN, J., CROSTACK, H., KAESE, V., PISCH, A., BECKMANN, F. and WINDHAGEN, H., 2006. *In vitro* and *in vivo* corrosion measurements of magnesium alloys. *Biomaterials*, **27**(7), pp. 1013-1018.
- WITTE, F., HORT, N., VOGT, C., COHEN, S., KAINER, K.U., WILLUMEIT, R. and FEYERABEND, F., 2008. Degradable biomaterials based on magnesium corrosion. *Current Opinion in Solid State and Materials Science*, **12**(5-6), pp. 63-72.
- WONG, H.M., YEUNG, K.W.K., LAM, K.O., TAM, V., CHU, P.K., LUK, K.D.K. and CHEUNG, K.M.C., 2010. A biodegradable polymer-based coating to control the performance of magnesium alloy orthopaedic implants. *Biomaterials*, **31**(8), pp. 2084-2096.
- WU, G., FAN, Y., GAO, H., ZHAI, C. and ZHU, Y.P., 2005. The effect of Ca and rare earth elements on the microstructure, mechanical properties and corrosion behavior of AZ91D. *Materials Science and Engineering: A*, **408**(1-2), pp. 255-263.

WU, W., PETRINI, L., GASTALDI, D., VILLA, T., VEDANI, M., LESMA, E., PREVITALI, B. and MIGLIAVACCA, F., 2010. Finite Element Shape Optimization for Biodegradable Magnesium Alloy Stents. *Annals of Biomedical Engineering*, **38**(9), pp. 2829-2840.

XIN, Y., HU, T. and CHU, P.K., 2010. Influence of Test Solutions on *In vitro* Studies of Biomedical Magnesium Alloys. *Journal of the Electrochemical Society*, **157**(7), pp. C238-C243.

YU, Y., WANG, J., LIU, C., ZHANG, B., CHEN, H., GUO, H., ZHONG, G., QU, W., JIANG, S. and HUANG, H., 2010. Evaluation of inherent toxicology and biocompatibility of magnesium phosphate bone cement. *Colloids and Surfaces B: Biointerfaces*, **76**(2), pp. 496-504.

YUN, Y., DONG, Z., LEE, N., LIU, Y., XUE, D., GUO, X., KUHLMANN, J., DOEPKE, A., HALSALL, H.B., HEINEMAN, W., SUNDARAMURTHY, S., SCHULZ, M.J., YIN, Z., SHANOV, V., HURD, D., NAGY, P., LI, W. and FOX, C., 2009. Revolutionizing biodegradable metals. *Materials Today*, **12**(10), pp. 22-32.

YUN, Y., DONG, Z., YANG, D., SCHULZ, M.J., SHANOV, V.N., YARMOLENKO, S., XU, Z., KUMTA, P. and SFEIR, C., 2009. Biodegradable Mg corrosion and osteoblast cell culture studies. *Materials Science and Engineering: C*, **29**(6), pp. 1814-1821.

ZBERG, B., UGGOWITZER, P.J. and LOFFLER, J.F., 2009. MgZnCa glasses without clinically observable hydrogen evolution for biodegradable implants. *Nat Mater*, **8**(11), pp. 887-891.

ZHANG, E., XU, L., YU, G., PAN, F. and YANG, K., 2009. In vivo evaluation of biodegradable magnesium alloy bone implant in the first 6 months implantation. *Journal of Biomedical Materials Research Part A*, **90A**(3), pp. 882-893.

ZHOU, W., SHEN, T. and AUNG, N.N., 2010. Effect of heat treatment on corrosion behaviour of magnesium alloy AZ91D in simulated body fluid. *Corrosion Science*, **52**(3), pp. 1035-1041.

ZIMMER, I., 2008-last update, **Materials Used in Orthopaedic Implants**. Available: <http://www.zimmerohio.com/ctl?template=PC&op=global&action=1&id=9480> [11/28/2012,